BRAIN
REVIEW ARTICLE

Quantitative myelin imaging with MRI and PET: an overview of techniques and their validation status

Chris W. J. van der Weijden,[1] Emma Biondetti,[2] Ingomar W. Gutmann,[3] Hildebrand Dijkstra,[4] Rory McKerchar,[5] Daniele de Paula Faria,[6] Erik F. J. de Vries,[1] Jan F. Meilof,[7,8] Rudi A. J. O. Dierckx,[1] Valentin H. Prevost[9] and Alexander Rauscher[5]

Myelin is the protective sheath wrapped around axons, consisting of a phospholipid bilayer with water between the wraps. The measurement of damage to the myelin sheaths, the evaluation of the efficacy of therapies aiming to promote remyelination and monitoring the degree of brain maturation in children all require non-invasive quantitative myelin imaging methods. To date, various myelin imaging techniques have been developed. Five different MRI approaches can be distinguished based on their biophysical principles: (i) imaging of the water between the lipid bilayers directly (e.g. myelin water imaging); (ii) imaging the non-aqueous protons of the phospholipid bilayer directly with ultra-short echo-time techniques; (iii) indirect imaging of the macromolecular content (e.g. magnetization transfer; inhomogeneous magnetization transfer); (iv) mapping of the effects of the myelin sheath's magnetic susceptibility on the MRI signal (e.g. quantitative susceptibility mapping); and (v) mapping of the effects of the myelin sheath on water diffusion. Myelin imaging with PET uses radioactive molecules with high affinity to specific myelin components, in particular myelin basic protein. This review aims to give an overview of the various myelin imaging techniques, their biophysical principles, image acquisition, data analysis and their validation status.

1 Department of Nuclear Medicine and Molecular Imaging, University of Groningen, University Medical Center Groningen, 9713 GZ Groningen, The Netherlands
2 Department of Neuroscience, Imaging, and Clinical Sciences, Institute for Advanced Biomedical Technologies, 'G. d'Annunzio' University of Chieti-Pescara, 66100 Chieti, Italy
3 Faculty of Physics, University of Vienna, 1090 Vienna, Austria
4 Department of Radiology, University of Groningen, University Medical Center Groningen, 9713 GZ Groningen, The Netherlands
5 Department of Pediatrics, University of British Columbia, Vancouver, BC V6T 1Z4, Canada
6 Department of Radiology and Oncology, Faculdade de Medicina da Universidade de Sao Paulo, Sao Paulo 05403-911, Brazil
7 Department of Biomedical Sciences of Cells and Systems, University of Groningen, University Medical Center Groningen, 9713 GZ Groningen, The Netherlands
8 Department of Neurology, Martini Ziekenhuis, 9728 NT Groningen, The Netherlands
9 CT-MR Planning division department, Canon Medical Systems Corporation, Tochigi 324-8550, Japan

Correspondence to: Chris W. J. van der Weijden
Department of Nuclear Medicine and Molecular Imaging, UMCG
Hanzeplein 1, 9713 GZ Groningen
The Netherlands
E-mail: c.w.j.van.der.weijden@umcg.nl

Received June 10, 2022. Revised September 30, 2022. Accepted November 07, 2022. Advance access publication November 21, 2022

Keywords: brain maturation; demyelination; MRI; myelin imaging; PET

Introduction

Myelin, a cellular membrane-like structure wrapped around axons, has neuroprotective effects, enhances neuronal signal conduction and supports axonal metabolism.[1–3] Myelin accounts for about 14% of the wet mass and 50% of the dry mass of brain white matter (WM)[4] and is generated by a wrapping of the cell membrane of oligodendrocytes around axons, creating a radial configuration. This radial configuration consists of lipids, proteins and fluids trapped between the myelin layers (both cytosolic and extracellular water, corresponding to the water in both the major dense and intraperiod lines, respectively). The non-aqueous major constituents of myelin are 70–80% lipids and 20–30% proteins, which is the reverse of the ratio found in other cell membranes.[1–4] Lipids act as an electric insulator, whereas proteins facilitate myelin compaction effects. Together, they enhance neuronal signal conduction, whereas myelin mitochondria are responsible for axonal metabolic support.[1–3]

In various neurodegenerative diseases, myelin is damaged, leaving the axons vulnerable to injury.[5] Therapies are currently in development, aiming to protect or even restore myelin and prevent axonal neurodegeneration.[6,7] However, to date, no remyelination therapy has passed phase III clinical trials. Remyelination therapy might be beyond the capabilities of a single agent due to the multifocal molecular processes involved in remyelination. Observed failure of efficacy in clinical trials may be due to a lack of an accurate biomarker for assessing de- and remyelination. Myelin imaging could provide such a biomarker and could thus be used to evaluate the efficacy of therapies. Furthermore, myelin imaging can also be used to monitor disease progression in demyelinating disorders and assess neurodevelopment.

MRI is the primary method for myelin imaging. In the MRI community, the water between myelin layers, consisting of both intra- and extracellular water, is referred to as myelin water. All other water is referred to as intra- and extracellular water (Fig. 1).[8,9] The main hydrogen pools relevant for MRI are CSF, free water within tissues and macromolecules (e.g. proteins).[8,9] CSF is located in the ventricles and the subarachnoid space. The free water within tissues comprises the intracellular fluid, e.g. cytoplasm, and extracellular fluid, e.g. interstitium, and, in the case of myelin, myelin water (Fig. 1). The macromolecules are primarily proteins within lipid bilayers, such as cell membranes or myelin. The different magnetic properties of these hydrogen pools can be used to characterize tissues with MRI.

Myelin imaging via PET exploits a radioactive tracer's binding affinity to proteins specific to myelin. The ionizing radiation emitted during the tracer's radioactive decay is detected and converted into maps of radiotracer concentration, providing an estimate myelin density.

This review aims to give an overview of MRI and PET methods for myelin quantification, with emphasis on techniques that have been validated against histology. In addition, some emerging techniques are addressed in the 'Discussion' section.

Magnetic resonance myelin imaging methods and their biophysical bases

The proton, which is the nucleus of a hydrogen atom, has an intrinsic spin and a magnetic moment. When biological tissue is subject to the MRI scanner's main magnetic field, the proton's spin can have two possible states, either low-energy or high-energy. At equilibrium, a slight abundance of spins is found in the low-energy compared to the high-energy state, resulting in a net bulk magnetization.[9,11] This intrinsic split into energy states is called the Zeeman effect. To acquire an MRI, radio-frequency (RF) pulses with a frequency that corresponds to the energy difference between the two states (resonance condition) are applied. Interactions between spins and their environment result in relaxation of the MRI signal. Spin-spin or 'transverse' relaxation is caused by dipole–dipole interactions between neighbouring spins, which results in slight resonance frequency variations. The exponential loss of coherence between spins due to this process is called T_2 relaxation. Mesoscopic or macroscopic field inhomogeneities further accelerate relaxation, with a characteristic time called T_2', resulting in a combined relaxation $R_2^* = 1/T_2^* = 1/T_2 + 1/T_2'$. An additional phenomenon, called longitudinal relaxation, denotes the loss of energy from the spin system caused by interaction with its surroundings. The time constant of this exponential return to thermal equilibrium is called the T_1 relaxation time. The additional application of spatially variable field gradients makes the resonance condition spatially dependent, enabling the creation of an image. Image contrast is generated by differences in T_1, T_2, T_2^* across tissues, as well as other parameters to which the MR signal can be sensitized.

Myelin MRI generally considers two hydrogen pools: the macromolecular pool, also known as the bound pool, and the free water pool (Figs 1 and 2).[8,9] CSF is often neglected in myelin imaging with MRI[8,13] because of the low amount of CSF in WM. The term 'bound' describes slow-moving, covalently bound-hydrogen atoms and water bound to macromolecules associated with a semisolid, macromolecular structure. In contrast, the free water pool consists of hydrogen atoms in water-rich environments, like cytoplasm and the extracellular matrix.[14] The free water pool can be further divided into myelin water, which is the water trapped between the myelin layers, and intra- and extracellular water.[8]

In the free water pool, the Zeeman order is the main process for restoring equilibrium in a magnetic field after RF excitation. However, in

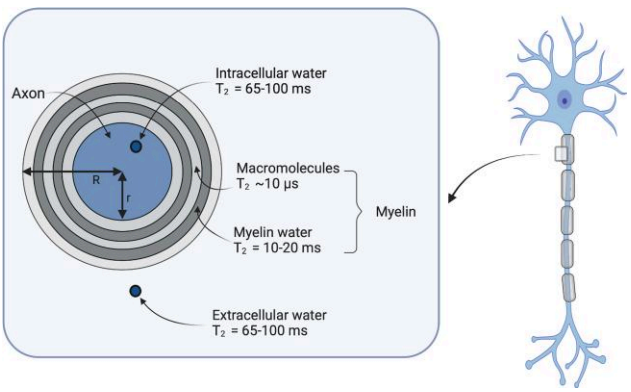

Figure 1 Representation of CNS characteristics relevant for myelin MRI. Myelin is wrapped around the axon. Within the axon is intracellular water, and outside the myelin layer is extracellular water. The myelin sheath consists of myelin water and lipid bilayers that contain macromolecules. Figure inspired by Fig. 1 from Campbell *et al.*[10]

myelin's compact structure, magnetic dipole–dipole interactions between neighbouring hydrogen atoms[15–18] also contribute to restoring magnetization to the equilibrium state.[9,11] Dipole–dipole interactions decrease rapidly with distance and are primarily intramolecular.[11] In the free water pool, the rapid orientation changes of atoms within molecules limit magnetic dipole–dipole interactions between molecules. However, the restricted motion of hydrogen in the bound pool formed by tightly packed myelin sheets, which contains both macromolecular bound hydrogen and lipid-bound-hydrogen atoms, enables intramolecular dipolar coupling of atoms within the same molecule.[9,11,14] The bound pool can therefore be subdivided into the Zeeman order, caused by the main magnetic field, and the dipolar order, derived from magnetic dipole–dipole interactions.[9,19] The dipolar order in the bound pool within myelin only interacts with the Zeeman order of the bound pool.[11,14,20] However, magnetization exchange also occurs between the Zeeman order of the bound-hydrogen pool and the Zeeman order of the free water-hydrogen pool. Such magnetization exchange occurs either through the migration of water molecules or spin exchange.[11,14] These phenomena can be exploited to isolate the dipolar order.

In a static magnetic field or when RF pulses are applied at the resonance frequency (Fig. 3), bulk hydrogen magnetization is exchanged between myelin water and intra- and extracellular water within the free water pool (Fig. 2).[8,21,22] In addition, hydrogen is exchanged between the free water pool and the bound pool. These exchange processes are in equilibrium. Disruption of the hydrogen exchange equilibrium by an off-resonance RF pulse (Fig. 3) leads to a net MT from the Zeeman order of the bound pool to the free water pool (removal of the dashed black arrow in Fig. 2).[13,23] However, a single off-resonance RF pulse (either negative or positive compared to the resonance frequency, Fig. 3) also results in magnetization exchange between the Zeeman order and the dipolar order of the bound pool, reducing MT (addition of the dashed grey arrow, Fig. 2).[11] A double-sided off-resonance RF pulse (both negative and positive compared to the resonance frequency, Fig. 3) can be used to eliminate the magnetization exchange between the Zeeman and dipolar order in the bound pool, which results in an enhanced MT from the Zeeman order of the bound pool to the free water pool (removal of the dashed grey and black arrows, Fig. 2).[23]

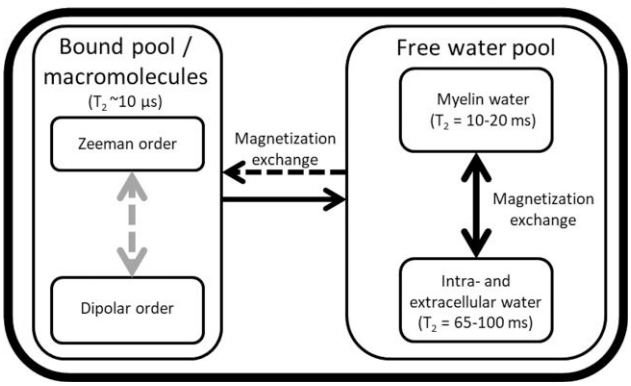

Figure 2 Schematic overview of MRI characteristics of the water pools in brain tissue. The free water pool can be subdivided into two compartments, myelin water and intra/extracellular water. Magnetization is exchanged between the bound pool and the free water pool. Within the free water pool, magnetization is exchanged between myelin water and intra- and extracellular water. The compartments have characteristic T_2 relaxation times, which are ~10 µs for the bound pool, 10–20 ms for myelin water and 65–100 ms for intra-/extracellular water.[12]

Five approaches have been used for myelin imaging with MRI: (i) imaging of the water pool between lipid bilayers directly (e.g. myelin water imaging, MWI); (ii) imaging of the non-aqueous protons of the myelin sheath's phospholipid bilayer component directly, using ultra-short echo-time (UTE) techniques; (iii) indirect imaging of the macromolecular content using magnetization transfer (MT) or inhomogeneous MT (ihMT) techniques; (iv) mapping of the effects of the myelin sheath's magnetic susceptibility on the MR signal using quantitative susceptibility mapping (QSM); and (v) measuring the effects of the myelin sheath on water diffusion. These five approaches are detailed next.

Myelin water imaging

The T_2 relaxation time of the water signal within different tissue compartments (Fig. 1) depends on the mobility of water molecules. In the confined space between the lipid bilayers, at a magnetic field strength of 3 T, the magnetization relaxes with a T_2 of 10–20 ms[24,25]; in contrast, in the intra- and extracellular water compartments, T_2 relaxation times at 3 T vary between 50 and 70 ms.[25] A MWI experiment samples the T_2 relaxation for 300 to 400 ms at 5–10 ms echo intervals, then decomposes the acquired signal into its relaxation components on a voxel-wise basis (Fig. 4).

MRI data acquisition for MWI needs to fulfil several criteria. First, sufficiently short echo times are needed to sample the relaxation of the short-lived myelin signal. On the other hand, echo times (TE) of several hundred milliseconds are required to sample the decay of intra- and extracellular water. Moreover, MT effects preclude multi-slice 2D acquisition. Due to these constraints, early work on MWI was done with a single-slice 2D scan.[8] With improved hardware and new rapid imaging techniques, 3D scans with more brain coverage could be acquired within a clinically acceptable duration. Parallel imaging using multi-channel coils allows for acceleration with a factor of three to four. By using a combined gradient echo and spin-echo scan (GraSE), further acceleration by a factor of three to five can be achieved.[26] Combining GraSE with parallel imaging allows for whole-brain coverage in ~10 min. A much simpler approach for the acceleration of data acquisition is compressed sensing,[26,27] albeit at high computational cost during reconstruction. In compressed sensing, the phase encoding steps are undersampled in a pseudo-random way, and the image is reconstructed under a sparsity constraint. Three-dimensional scans allow for high acceleration factors of five to ten due to the two-phase encoding directions, allowing for whole-brain MWI in well under 8 min.[28] Compressed sensing allows for shorter echo spacing than GraSE because it does not require an echo-planar readout. In principle, the compressed sensing concept can be extended to the echo dimension for further acceleration. The large number of refocusing pulses needed for MWI results in a high specific absorption rate. Therefore, there is a lower limit for the repetition time that can be used. For a 48-echo scan at 3 T, repetition times are around 1 s. The much higher specific absorption rate at 7 T requires longer repetition times.[29] Furthermore, the T_2 relaxation times are shortened with increasing field strength. Initial work in human MWI at 7 T used the GraSE approach,[29] but it is anticipated that compressed sensing approaches will be more successful at ultra-high fields. Scan time and specific absorption rate can also be reduced by skipping the refocusing pulses altogether and using a multi-gradient echo acquisition,[30] albeit at the cost of increased influences from background field inhomogeneities.

The multi-echo signal needs to be decomposed into its individual components, which is typically done with a non-negative

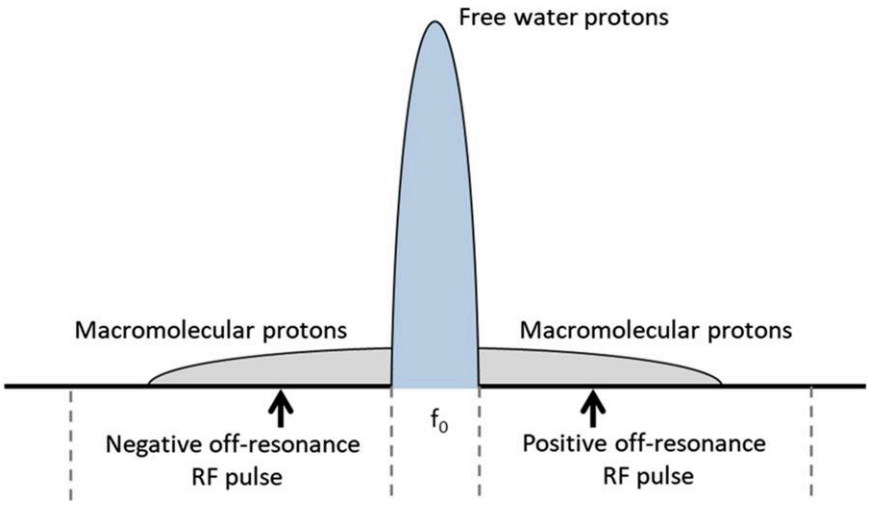

Figure 3 Hydrogen precession frequency spectrum. The precession of free water protons is centred closely around the resonance frequency (f_0). On the other hand, the precession of macromolecular protons is spread over a broad spectrum and can therefore be saturated with RF pulses at negative and positive off-resonance frequencies.

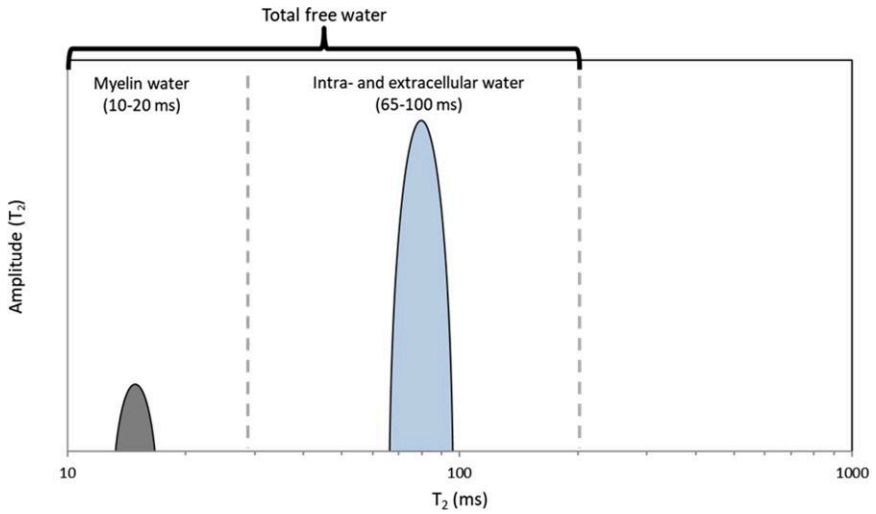

Figure 4 T_2 spectrum used to estimate the MWF. On the y-axis is the T_2 amplitude, on the x-axis the T_2 relaxation time. The MWF is calculated as the ratio of myelin water and total free water.

least-squares approach.[31] This method assumes the measured signal is the sum of individual signals, each decaying with a specific relaxation time, with coefficients corresponding to the number of spins within a voxel with that particular relaxation time. Such a signal decomposition results in a spectrum of relaxation times. The myelin water fraction (MWF) is then the area under the short relaxation times divided by the area under the entire spectrum. The cut-off between short and long relaxation times is subject to user interaction. At 3 T, it is recommended to set the cut-off to 25 ms.[32] Note, however, that this cut-off may depend on the person's age or disease status or on the fixation status of post-mortem tissue.[33] As a general rule, publications should show representative distributions to justify the chosen cut-off. A freely available software package can perform the non-negative least-squares fitting, including the correction for stimulated echoes[34,35] in <30 s.[36] The signal-to-noise ratio of MWI is inherently low because the MWF is ~10%, and myelin water's relaxation time is relatively short at 10 ms. Therefore, the myelin signal decays quickly, and with an echo spacing of 8 to 10 ms, the myelin signal drops below the noise level by the fifth echo. Therefore, small changes in myelin are challenging to detect, especially in demyelinated tissue or not yet myelinated neonate tissue.[8,25] To date, only one study has reported MWF in multiple sclerosis lesions.[37] It is instructive to read the work on luminal water imaging, which is based on the same idea of multi-compartment relaxation. In luminal water imaging, the relaxation times are much longer, which makes data acquisition and analysis more robust.[38,39]

T_1 relaxation, T_1- and T_2-weighted imaging

Early studies on myelin imaging have used single exponential T_1 and T_2 relaxation times to assess myelin density (Table 1), but these parameters have shown only moderate correlation with histological staining for myelin (T_1: $R^2 = 0.48$; T_2: $R^2 = 0.45$).[46] T_1-weighted (T_1w) and T_2-weighted (T_2w) scans are regularly used in the clinic to detect structural abnormalities. Because myelin shortens T_1

and T_2 relaxation times, the T_1w signal increases with increasing myelin content and the T_2w signal decreases with increasing myelin content. This observation has led to the suggestion that the ratio of a T_1w and a T_2w scan should be particularly sensitive to myelin content.[47] No histological evidence has yet been presented to validate the T_1w/T_2w results, and the correlation between T_1w/T_2w and MWI is poor.[48,49]

Multi-component driven equilibrium single pulse observation of T_1 and T_2 (mcDESPOT) incorporates both T_1 and T_2 measurements.[22,50] For measuring T_1 and T_2, the mcDESPOT approach uses a spoiled gradient echo and a balanced steady-state free precession sequence.[51] By focusing on the short T_1 and T_2 relaxation times, a proxy for the MWF can be generated. However, due to the dependence on a balanced steady-state free precession sequence for measuring T_2, mcDESPOT is susceptible to MT effects and has therefore been shown to be imprecise for MWF measurement.[22,50] In addition, no histological validation has yet been published for the myelin content estimates from mcDESPOT.

Another method that exploits the different T_1 relaxation times of water compartments is direct visualization of the short transverse relaxation time component (ViSTa).[52] This technique uses two inversion pulses with optimized spacing to suppress long T_1 signals from the intra- and extracellular spaces. The remaining signal has a short T_2^* in the range of myelin water (10 ms). An apparent MWF is computed by dividing the ViSTa signal by the separately acquired proton density (PD)-weighted gradient echo signal and multiplying this by a scaling factor accounting for T_1 and T_2^* weighting. ViSTa with segmented echo-planar readout allows for whole-brain coverage within 7 min.[53]

Synthetic MRI

Synthetic MRI is an umbrella term for quantitative MRI maps calculated from a series of images using Bloch–Torrey simulations.[54] The QRAPMASTER method uses a multi-echo-time (TE), multi-delay time (TD) saturation recovery spin-echo sequence.[40] Multiple echoes enable T_2 estimation, and multiple delay times enable T_1 estimation, subsequently permitting the estimation of transversal magnetization (M_{xy}), PD and the RF field (B_1). With these parameters, synthetic images with different T_1, T_2 and PD weighting can be computed retrospectively. The minimal TE of QRAPMASTER is too long to measure the short T_2 of myelin water directly. However, multi-component voxel models can be used, composed of myelin, cellular water, free water or excess parenchymal water,[21] each with unique PD and T_1 and T_2 relaxation properties and without further assumptions on interacting pools within each compartment. Determining the contributions of the three non-myelin water compartments to a voxel's signal enables the estimation of the myelin volume fraction (MVF), as all four compartments together should add up to 100%. The original QRAPMASTER sequence takes 5 to 9 min to run. With the 'Quantification using an interleaved look-locker acquisition sequence with a T_2 preparation pulse' sequence, 3D isotropic whole-brain images can be acquired within 11 min.[41]

Ultra-short echo-time imaging

In addition to free water protons, the myelin sheath contains protons in the macromolecules with very short T_2 relaxation times linked to dipole–dipole interactions of motion-restricted hydrogen atoms in the bound pool.[42] With T_2 relaxation times in the range of 10 µs,[43] the macromolecular MR signal decays too fast for imaging with conventional MRI techniques.[43] UTE MRI sequences were therefore developed to directly measure the bound proton pool in the brain (Fig. 2).[44,45,55]

The data acquisition strategy for rapidly decaying signals is to suppress the long-living signals and image the signal of interest with extremely short echo times. Signal suppression is typically accomplished by an adiabatic inversion pulse,[56] which inverts the long T_2 spin populations but saturates those with short T_2. After an inversion time (TI), the saturated spins have largely recovered and the long T_2 spins are nulled. Subsequent dual-echo imaging module with an ultra-short TE and a longer TE acquires a reduced signal from long T_2 protons in both echoes. Finally, the second echo, containing only the long T_2 signal, is subtracted from the first echo to create a map of short T_2 protons.

Myelin imaging with UTE requires efficient suppression of long T_2 WM signal, which depends on the selection of TI. The appropriate TI depends on T_1, which varies within the brain and across individuals (Table 1).[57,58] Various variants of inversion recovery UTE have been developed, for which dual-echo sliding inversion recovery (DESIRE)-UTE and short repetition time (TR) adiabatic inversion recovery (STAIR)-UTE seem to be the most promising.[59,60] The DESIRE-UTE deals with the TI problem by generating a series of TIs, and thereby efficiently nulls WM signal throughout the brain irrespective of its T_1.[60,61] STAIR-UTE uses a shorter TR to increase the efficiency of suppressing long T_2 components with a broad range of T_1.[59] Typical UTE sequence durations for human full brain coverage are between 5 and 10 min.[59,62,63]

Magnetization transfer

The very fast relaxation of macromolecular protons corresponds to a broad spectrum in the frequency domain. Therefore, off-resonance pulses can saturate the macromolecular content without affecting water protons, which have a very narrow spectrum (Fig. 2 and 3). MT from the bound pool to the free water pool will partly saturate the free water pool, resulting in a lower measured signal.[13,64,65] The quantity of interest in this phenomenon is called the MT ratio (MTR) and assumes that the most abundant macromolecular content within the CNS is from myelin. The MTR is the difference between saturated magnetization using off-resonance frequency pulses (M_s) and magnetization using no prepulse (M_0) divided by M_0

$$\mathrm{MTR} = (M_0 - M_s)/M_0 \quad (1)$$

A high density of macromolecules increases the MTR due to increased MT to the free water pool.[64] However, MTR is also dependent on acquisition parameters, such as the shape, amplitude, duration and offset frequency of the MT pulse. The image acquisition schemes that follow the MT prepulse are usually spoiled gradient echo sequences. Off-resonance RF pulses with an offset frequency of 7–10 kHz result in optimal saturation. Clinical sequences generally have an offset frequency below 2 kHz due to hardware restrictions, resulting in sub-optimal saturation.[66]

The quantitative MT (qMT) approach uses the binary spin bath model to estimate the fraction of protons bound to macromolecules, called the bound proton fraction (fB), and the ratio of the number of bound molecular protons to the free protons, called the pool size ratio. Several MT images obtained using different frequency offsets and powers were initially needed to fit the model,[67] but a more recent methods using a single offset generates 3D

Table 1 Single exponential T_1 and T_2 relaxation times at 1.5 and 3 T[17,40–45]

	1.5 T		3 T	
	T_1 (ms)	T_2 (ms)	T_1 (ms)	T_2 (ms)
CSF	3700–5127	1910	3817–6873	
References	Warntjes *et al.*,[40] Boucneau *et al.*,[43] Du *et al.*[45]	Warntjes *et al.*[40]	Boucneau *et al.*,[43] Waldman *et al.*[44]	
GM	998–1260	78–95	968–1820	71–109
References	Warntjes *et al.*,[40] Horch *et al.*,[42] Boucneau *et al.*,[43] Du *et al.*[45]	Warntjes *et al.*,[40] Horch *et al.*,[42]	Horch *et al.*,[42] Boucneau *et al.*,[43] Waldman *et al.*[44] Du *et al.*[45]	Horch *et al.*,[42] Waldman *et al.*[44]
WM	560–884	72–79	750–1110	56–75
References	Warntjes *et al.*,[40] Horch *et al.*,[42] Boucneau *et al.*,[43] Waldman *et al.*[44]	Warntjes *et al.*,[40] Horch *et al.*[42]	Horch *et al.*,[42] Boucneau *et al.*,[43] Waldman *et al.*[44] Du *et al.*[45]	Horch *et al.*,[42] Waldman *et al.*[44]
Water associated with macromolecules	~4000	~0.001	–	–
References	Bloembergen *et al.*,[17] Fujita *et al.*[41]	Bloembergen *et al.*,[17] Fujita *et al.*[41]		

maps in a relative short acquisition time.[68] However, this model ignores some important components of semisolid structures, such as myelin, resulting in imperfect modelling of the MT effects.[69]

In fact, for semisolid structures such as myelin, the high concentration of lipids and the specific configuration of myelin generate a dipolar order (Fig. 2). This dipolar order is part of the bound pool and is coupled with the Zeeman order when off-resonance RF saturation is applied (Fig. 2, dashed grey arrow).[20,70] As the dipolar coupling decreases rapidly with distance, it is strongest between the two hydrogen nuclei within a single water molecule.[71] In a perfect liquid system, the rapid molecular diffusion creates spatial and temporal averaging of the dipolar coupling, making the dipolar order irrelevant. In the case of myelin, the high concentration of methylene groups composing the long lipid chains, and their strong motion restriction due to the multilamellar myelin configuration, enable inter- and intramolecular dipolar coupling associated with incomplete motion averaging, leading to the creation of a dipolar order.[9,14,23,71,72] The dipolar relaxation time T_{1D} of human myelin was estimated *in vivo* as a single component in the range of 5–10 ms.[14] Recent work on *ex vivo* spinal cord tissue proposed a bi-component T_{1D} model, with a short and long myelin T_{1D} on the order of 0.5 and 10 ms, respectively.[19]

When RF saturation is applied at one offset frequency, dipolar and Zeeman orders of the bound pool are coupled and exchange their magnetization (Fig. 2, dashed grey arrow).[73] In practice, the dipolar order is opposed to the Zeeman saturation, making the MT from the bound pool towards the free water pool less efficient. Nevertheless, when the saturation is applied at similar offsets simultaneously (or 'dual offset saturation') with similar energy, a decoupling between the dipolar and Zeeman orders occurs, which removes the dipolar order opposition and makes the RF saturation more efficient (Fig. 2, removal of the dashed grey arrow).[20,70] Due to the application of a double-sided off-resonance RF pulse, the contributions of the dipolar order are averaged out, causing the net magnetization exchange of the dipolar order with the Zeeman order to be zero. Hence, decoupling of the dipolar order occurs, allowing isolation of the dipolar order to subsequently obtain images weighted by T_{1D}.[14,74]

The ihMT approach[9,23,72] has been developed to exploit these mechanisms to specifically isolate the myelin signal.[74,75] Using several MT images, with single and double-sided off-resonance saturation (Fig. 3), ihMT ratio (ihMTR) maps can be generated as

$$ihMTR = \frac{S^{+}+S^{-}-2S^{dual}}{S_0} \quad (2)$$

with S^{+} and S^{-} the MT signal obtained after a single offset saturation at a positive and negative frequency, respectively, S^{dual} the MT signal obtained after a dual offset saturation at the same energy, and S_0 the reference signal obtained without saturation. This double subtraction has been proposed to minimize the MT asymmetry effects, especially at high magnetic fields.[76] Note that a closely related formalism has also been proposed based on the original definition of MTR, but introducing a factor 2 in the denominator.[71,77]

By definition, ihMT is sensitive to the T_{1D} of the dipolar order and its myelin specificity could be enhanced by applying RF pulses focused on long T_{1D} values that are related to myelin.[74,78] The sensitization of the ihMT signal to a given T_{1D} value is driven by power, offset frequency and timing parameters of the RF irradiation.[19,74] For example, higher RF power tends to increase all T_{1D} values. This not only leads to an overall increase in the ihMT signal, but also to a contrast reduction between short and long T_{1D} components.[19,74] On the other hand, time intervals separating the saturation pulses of dual offset saturation acquisitions can act as a T_{1D}-filter, removing the short T_{1D} contribution and improving myelin specificity at the cost of lower sensitivity.[11,19,78]

Quantitative susceptibility mapping

Magnetic susceptibility is an intrinsic tissue property that describes the change in magnetization of a material in response to an applied magnetic field.[79,80] This change leads to local variations in the magnetic field and, therefore, spin resonance frequency. According to their local resonance frequency, spins accumulate a phase difference during the time between excitation and sampling, which is reflected in the phase of gradient MRI scans.[81] Biological tissues can be either diamagnetic or paramagnetic depending on their molecular contents and microstructure. In the brain, iron is the dominant

source of paramagnetic susceptibility, and myelin and calcifications are the most important diamagnetic substances.[82] The lipids and proteins in the myelin sheath are major contributors to the myelin's diamagnetic susceptibility.[79] Therefore, magnetic susceptibility is considerably affected by changes in myelin density. Areas of demyelination, such as multiple sclerosis lesions, demonstrate an increase in magnetic susceptibility due to the removal of diamagnetic myelin.[83–85]

Data for QSM are acquired with a 3D gradient echo scan, usually with multiple echoes that range from 5 to 30 ms at a magnetic field strength of 3 T.[86] Flow compensation can be used for more accurate measurements of magnetic susceptibility in veins, although on clinical systems full flow compensation is only achieved for single-echo scans. Under specific scanning and image processing conditions, an adequate level of flow compensation for multi-echo sequences at 3 T can be obtained using dipolar read gradients.[87] The scanning protocol for QSM is fast (<3 min for 1 mm isotropic resolution) and widely used clinically in the form of (qualitative) susceptibility-weighted imaging (SWI). Thus, it is readily available on almost all MRI scanners. However, SWI uses high pass filtered phase images, and usually the original phase images required for QSM are discarded. Although the full phase could be recovered using machine learning,[88] it is recommended that the scanner is explicitly instructed to save the unfiltered phase images for further processing into QSM.[82]

The modification of the magnetic field created by a spatial distribution of magnetic susceptibilities can be computed as the convolution of the susceptibility distribution with a magnetic unit dipole. However, the phase image only contains information on the underlying tissue magnetic susceptibility, but also effects from background field inhomogeneities, i.e. magnetic field variations induced in the brain by external sources and unwanted phase accrual from scanner drift and eddy currents. Moreover, phase wraps, i.e. 2π aliasing, are almost always present in these images and need to be removed, followed by the removal of the background field. Deconvolution with the unit dipole solves an ill-posed inverse problem of computing the magnetic susceptibility from the local field. The QSM processing pipeline is not yet fully standardized, and there are various methods for each processing step. QSM is still mainly computed offline, and various toolboxes are available.[89–91]

Diffusion MRI

The aim of diffusion MRI is to sensitize the MRI signal to the diffusion of water molecules.[92,93] This is accomplished by applying diffusion sensitizing field gradients in multiple spatial directions. Diffusion sensitization consists of a field gradient along a specific direction, followed by a 180° pulse, followed by the same gradient. Stationary spins are refocused by the 180° pulse, whereas spins that travel along the gradient direction experience different field strengths before and after the pulse and, therefore, a loss of coherence, i.e. a reduction in signal, relative to a reference diffusion-encoding-free scan. The gradient strength and duration jointly determine the degree of sensitivity to diffusion and are described by a parameter called the *b*-value, typically ranging from 700 to 1500 s mm^{-2}. By applying diffusion sensitizing gradients along several directions, typically 32 to 64, one can measure the diffusion tensor, which describes the diffusion along different spatial directions. Diffusion data are most commonly acquired using spin-echo echo-planar imaging, which allows for rapid acquisition of diffusion-sensitized images along many spatial directions, as well as reference images.

Geometrically, the tensor can be represented as an ellipsoid.[94] For free water, diffusion is isotropic and unrestricted, and the tensor is a sphere. For isotropic tissues, the probability of water molecules encountering tissue boundaries is the same in all directions, and the resulting tensor is also a sphere but with a reduced radius. For anisotropic tissues, such as nerve fibres, water diffuses more strongly along the direction of the fibre than perpendicular to the fibre direction, wherein the water molecules encounter tissue barriers that result in anisotropic diffusion. The ellipsoid is therefore elongated along the direction of strongest diffusion. Mathematically, the diffusion tensor is described by its eigenvalues and eigenvectors, determined by fitting a diffusion model to the acquired data. The largest eigenvalue is associated with the eigenvector that points to the strongest diffusivity direction. In the brain's WM, this direction is along the axons' main axis. From these eigenvalues, one can compute various metrics to describe a tissue's diffusion properties. The mean diffusivity (MD) is the average of the eigenvalues. The fractional anisotropy (FA) is the normalized standard deviation of the eigenvalues, which ranges between 0 and 1. FA is low for isotropic tissues and increases with anisotropy.

Several structural components in WM influence water mobility and give rise to the anisotropy in the diffusion-sensitized signal. The myelin sheaths, axonal membrane and neurofibrils (neurofilaments, microtubules) within each axon, are three longitudinally oriented structures that impact diffusion.[95–98] Beaulieau and Allen[95,96] investigated the respective roles of myelin and microtubules in anisotropic diffusion by measurements in excised myelinated and non-myelinated nerves from garfish and by depolymerizing the microtubules that are required for fast axonal transport. By systematically separating the effects of myelin, microtubules and neurofilaments on anisotropy, they confirmed that the axonal membrane is the main structure that causes anisotropic diffusion in WM. Diffusion anisotropy was only weakly influenced by the presence or absence of myelin, as the degree of anisotropy was similar for the three nerve types. The presence of diffusion anisotropy drivers other than myelin is also consistent with the range of findings from diffusion imaging in multiple sclerosis lesions, indicating that the value of diffusion-weighted MR for detecting demyelination is still inconclusive.[99]

Like all MRI techniques, diffusion tensor imaging (DTI) is affected by partial volume effects. If a voxel contains fibres running in different directions, the overall FA will be low, even though the individual tracts may cause a high FA. The spatial resolution of a diffusion scan is typically in the range of 8 to 16 mm^3. Depending on the scan's spatial resolution, 50 to 70% of voxels may contain crossing fibres.[100] Because of its wide availability, DTI has been studied in various diseases.[101,102]

Advanced diffusion techniques, such as neurite orientation dispersion and density imaging,[103] WM tract integrity[104] and diffusion basis spectrum MRI,[105,106] can estimate the intra- and extra-axonal diffusivity (for a thorough description, see Novikov *et al.*[107]) and differences between these two quantities are thought to be sensitive to myelin integrity. With intact myelination, there should be no difference between intra- and extra-axonal diffusivity, but with myelin damage, the extra-axonal diffusivity is slightly increased compared to intra-axonal diffusivity and can thus be used as a proximal marker for myelin integrity.

When both a diffusion and a myelin-sensitive scan are available, a measure of relative myelin thickness, the *g*-ratio, can be computed.[10,108–110] The *g*-ratio is the axonal radius (*r*) divided by

the radius of the axon, including the myelin sheath (R), which can be derived from the MVF and the axonal volume fraction (AVF) as: $g = r/R = (1 + MVF/AVF)^{-1/2}$. The MVF can be estimated from MWF, f_B or pool size ratio. Since each of these measures captures only the myelin water or the semisolid component of the myelin sheath, a calibration factor is needed to compute MVF from these values.[109,111] Therefore, the summation of myelin macromolecule volume estimated with ihMT and the myelin water volume estimated with MWI would accurately estimate the total MVF. The axonal water fraction (AWF) can be determined by dividing the intra-axonal diffusivity by the summation of intra- and extra-axonal diffusivity. Subsequently, the AVF can be calculated according to the following formula: AVF = (1 − MVF)AWF.[108] However, in this formula, the contribution of other biological phenomena (e.g. macromolecules, extracellular fluid) to the MRI signal, aside from myelin and axons, is neglected.

The open-source tool NiftyFit can estimate the *g*-ratio based on T_2 relaxometry data for the MVF and neurite orientation dispersion and density imaging or DTI for the AVF.[108,112] Nonetheless, the many different ways in which MVF and axonal water fraction are measured make comparison of studies difficult.

PET

PET uses radiopharmaceuticals, which are molecules specific for certain biological or physiological phenomena that are labelled with a radioactive atom (e.g. ^{11}C, ^{18}F).[113,114] As the radioactive atoms of the PET tracer decay, they emit positrons that annihilate with nearby electrons. This annihilation causes the release of two gamma rays in opposite directions, which are detected by the PET scanner. For ^{11}C tracers, an onsite cyclotron and radiochemistry laboratory is required due to the short half-life (~20 min), whereas for ^{18}F tracers this is not required as the longer half-life (~110 min) enables transport to nearby centres. All PET tracers for brain imaging have to be lipophilic to cross the blood–brain barrier. However, a suitable brain PET tracer should have a much higher affinity to their target than to lipids. Moreover, the amount of tracer is low relative to the number of target binding sites. This means that for suitable brain PET tracers almost all tracer binds to the target and only a small proportion ends up within cellular lipid membranes. To determine this for a PET tracer, blocking studies should be performed in which the target is saturated, and hence both the binding affinity of the tracer and the amount of non-specific binding (e.g. proportion trapped within lipid membranes or low affinity binding to other molecules) can be determined.

As myelin layers are composed of lipids and proteins, a radiotracer that binds specifically to one of these components could be used for myelin imaging. Myelin basic protein (MBP) is such a molecule.[115] When myelin gets damaged, MBP loses its beta sheet structures, which are the binding targets for several PET radiotracers. The loss of binding sites for the tracer can therefore be used to capture the demyelination processes.[116] Various PET radiotracers have been evaluated for myelin imaging.[117–119] These PET radiotracers were originally designed to bind to beta sheet structures within amyloid depositions in the brain's grey matter (GM), which are typically found in Alzheimer's disease. However, studies showed that amyloid radiotracers also bind to the beta sheet structures of MBP, and therefore these radiotracers were repurposed for myelin imaging.[120] Furthermore, diagnosis of demyelinating disorders occurs normally at a younger age, than the onset of amyloid plaque deposition, a phenomenon found in individuals with Alzheimer's disease.[121] When amyloid plaque deposition occurs, tracer accumulation will increase in the cortical area, whereas in case of myelin damage, the beta sheet structure will be compromised, reducing tracer binding.[122] In addition amyloid deposition occurs in GM, whereas myelin damage is mostly measured in WM. While there is considerable contribution of GM pathology in multiple sclerosis,[123] MRI has difficulties measuring the low cortical myelin content. PET has already been shown to be able to measure myelin content in the GM reliably,[124] but whether this is also the case for GM lesions still remains to be investigated. Furthermore, the comorbidity of Alzheimer's disease and multiple sclerosis is rare, as current literature reports primarily case studies.[125] Therefore, the risk of confounding results is low. A different class of radiotracers, called diaminostilbenes, was specifically developed for myelin imaging. Among these tracers, ^{11}C-MeDAS (C-11-labelled *N*-methyl-4,4′-diaminostilbene) has shown promising results in animals for visualization and quantification of de- and remyelination processes.[124,126,127] Myelin tracers with a similar structure to ^{11}C-MeDAS have shown to bind to the beta sheet structure of intact MBP.[128,129] As such, it is likely that ^{11}C-MeDAS also binds to MBP. During demyelination, the beta sheet structure of MBP disintegrates, resulting in a reduction in the number of binding sites for ^{11}C-MeDAS. However, until *in vivo* blocking studies have been performed to saturate MBP, the amount of non-specific binding and whether ^{11}C-MeDAS truly binds to MBP remains debatable. Nonetheless, a competition binding assay of MeDAS in isolated myelin fractions using ^{3}H-BMB (a PET tracer with MBP binding affinity) as the radioligand, resulted in an inhibitory constant (K_i) value of 126 nM, while MeDAS did not show any specific binding to isolates that were devoid of myelin.[128,130] Furthermore, MeDAS itself has fluorescent properties and when *ex vivo* fluorescence microscopy of mouse brain was compared with immunohistochemical staining of MBP, the staining patterns were virtually identical.[128,131] A first-in-human study with ^{11}C-MeDAS also showed with ^{11}C-MeDAS PET differences in myelin density per lesion type in agreement to a radiologically validated myelin density score, which is as yet the first of its kind.[124] However, it is unclear whether this tracer can also bind to beta sheets in amyloid plaques. There are no other PET tracers that target a different protein or component of myelin, aside from MBP.

Another class of PET tracers under development aims to evaluate the result of demyelination rather than myelin itself. Brugarolas *et al.* evaluated PET tracers targeting axonal potassium channels, which are upregulated in the case of demyelination.[132,133] The advantage of this kind of tracer would be the increased tracer uptake in case of demyelination, which could facilitate the detection of demyelinated lesions. However, further studies and validation are still needed.

For absolute quantification, the amount of radiotracer in arterial blood is continuously measured during a dynamic PET scan, and blood samples are drawn for calibrating the blood curve to estimate the blood/plasma ratio, and to determine the amount of intact (unmetabolized) radiotracer.[134] For accurate PET imaging, blood sampling is required to determine what part of the tracer is still in blood and what part is within tissue, to enable estimation of specifically bound tracer. However, for some tracers, a reference tissue devoid of specifically bound tracer may be used. This method does not require blood sampling and only minimally affects PET quantification of specifically bound tracer. If tracer kinetics allow, a brain PET scan could take only 10–20 min without the use of blood sampling, which would be much more applicable for routine clinical use. In such cases, the standardized uptake value, which is the

total uptake of tracer in both blood and tissue in a particular region of interest, corrected for bodyweight and net injected dose, can be used for quantification. However, standardized uptake value is highly susceptible to hemodynamic effects that affect tracer delivery, which makes this parameter less reliable for longitudinal follow-up or treatment monitoring. An anatomical 3D T_1w MRI scan is usually acquired to provide anatomical context of the radiotracer map. The complicated nature of quantitative PET requires extensive expertise in proper data handling and data analysis. Recent developments for direct generation of parametric maps of the radiotracer distribution during PET image reconstruction may contribute to their routine clinical use.[135,136] For quantitative PET analysis, several open-source (e.g. 3D Slicer[137]) and commercial software packages (e.g. PMOD) are available, which combine the information from the PET images and blood samples.

Validation of myelin imaging methods

Approaches to the validation of an MRI technique span a wide range, and can include MRI-histology correlation, studies in animal models and studies in humans, undertaken ideally across several independent research groups. While histopathology, in particular with electron microscopy (EM), is seen as the gold standard for validation of imaging techniques, several factors influence histological quantification, including the effects of fixative agents, post-mortem interval and tissue handling.[138–141] Discrepancies between studies may also arise from the method used in histological quantification: EM, immuno-histology and chemical-histology. The concentration of tissue iron, a potent modifier of the MRI signal, is reduced by fixation.[142] Furthermore, MRI parameters, such as T_1, T_2 or MTR, may change due to fixation.[143–146] It should be kept in mind that high correlations between MRI and histopathological measures of myelin are necessary but not sufficient evidence of specificity. For mcDESPOT, T_1w/T_2w, multi-component T_1, MR fingerprinting, VISTA and MR elastography, no histological validations have been published yet. These techniques are not discussed further.

Most validation studies use densitometry of luxol-fast blue (LFB)-stained sections for myelin quantification. LFB is a lipophilic dye that stains both intact myelin and unphagocytosed myelin debris.[147,148] Sections can be as large as entire brain hemispheres.[149] However, the staining can vary spatially and between samples, limiting the calibration of optical density assessments and the pooling of results from several tissue samples.[150] The gold standard for histology of myelin is EM with segmentation of the myelin and non-myelin tissue. Drawbacks of EM are the segmentation step and the small field of view, which may not be representative for the tissue of interest, and uncertainties in the definition of the inner and outer boundaries of the myelin sheath. Tissue shrinkage during embedding is <10%[151,152] and, assuming that the shrinkage is proportional to the compartmental water content, the error due to differential shrinkage should be small.[153] The ideal myelin imaging technique would be specific and sensitive to myelin, have high reproducibility and be easy to implement. While none of the techniques addressed herein fulfil all these criteria, each of them may be useful for particular applications.

Validation studies investigate the biophysics underlying the MR signal rather than on the scanning method. Studies in animals and tissue samples often use high field strengths, numerous averages resulting in long scan times, and scan parameters that are often not feasible in human studies. In a clinical setting, the scan time and the technical feasibility of scan parameters play an important role. In the following, we give an overview the MRI techniques' validation status, highlighting a few important studies for each technique, and we discuss pitfalls and confounders. We also present selected applications in humans that further validate the MRI techniques. For overviews of validation studies, we refer the reader to other publications.[46,154–158]

In a total of 20 mice at different stages of de- and remyelination due to a cuprizone diet, the correlation between MTR measured *in vivo* and LFB staining for myelin was $R^2 = 0.77$.[159] In a total of 15 mice (six controls, and three each from a dysmyelination, a hypomyelination and a hypermyelination model) at 15.2 T, West *et al.*[153] determined a correlation between MVF from EM and MT of $R^2 = 0.70$, which is in good agreement with studies in *ex vivo* human multiple sclerosis brain tissue (total $n = 77$)[143,160–162] and brain tissue of 15 patients with X-linked adrenoleukodystrophy.[163] *In vivo* studies in multiple sclerosis found that MTR is decreased in multiple sclerosis lesions but also in diffusely abnormal white matter (DAWM) and normal-appearing white matter (NAWM)[164] and that MTR was associated with disease duration and disability scores in multiple sclerosis.[165] MTR remained stable in 20 multiple sclerosis patients treated with alemtuzamab but decreased in the untreated control group of 18 patients.[166] In 16 fixed multiple sclerosis brains and four controls, myelin immunostaining intensity was the best correlate of MTR in a multivariate model.[167] The distinction of tissue that is demyelinated and tissue that has undergone both demyelination and axonal loss is important for assessing the capacity for remyelination.[162] However, both MTR and the bound pool fraction are non-zero in non-myelinated tissue, which is due to the technique's inability to distinguish between myelin- and non-myelin-macromolecules.[143,153,161,168] MTR is also sensitive to inflammation and oedema.[169–171] In animal studies of inflammation, MTR was more affected by inflammation than by variations in myelin.[170,172] Vavasour *et al.*[171] found a correlation between water content and MTR of $R^2 = 0.42$, further suggesting that inflammation and oedema alter MTR. In an animal model of multiple sclerosis, MTR decreased before any signs of decreased myelin content, suggesting that these changes are more probably due to inflammatory events than demyelination.[173] Finally, MTR is also influenced by tissue iron concentration and increases by 34% after chemical iron extraction.[174,175] Poor correlations between iron staining and MTR (e.g. $R^2 = 0.02$ in Wistar rats[176]) may be due to the low iron content in rodent brain compared to humans.[177–180] Furthermore, animal models of dysmyelination may have different brain iron concentrations than the wild-type.[179]

Advanced MT approaches are qMT and ihMT. In the corpus callosum of 22 cuprizone-fed mice and 13 controls, the correlation was $R^2 = 0.35$ between qMT and myelin histology with anti-MBP and $R^2 = 0.55$ between qMT and Black Gold II as a measure for myelin.[181] In contrast, in nine rats in a glioma model, an R^2 of 0.79 to 0.94 was observed using LFB for myelin histology,[182] and in another study assessing 15 cuprizone-fed mice and eight controls, R^2 ranged from 0.76 to 0.83 between qMT and anti-MBP staining.[183] Similar observations were made in post-mortem tissue of multiple sclerosis patients, albeit with slightly lower correspondence between qMT and myelin histology with LFB ($R^2 = 0.52$–0.64).[143,161] In patients, qMT was decreased in multiple sclerosis lesions,[184] and myelin density measured with qMT was associated with disease duration and disability in multiple sclerosis.[185] While qMT seems more specific to myelin than MT, it requires longer scan times and complex data processing for model fitting.[186] So far, there is no consensus on the optimal model for parameter quantification in qMT. Furthermore, qMTI is sensitive to oedema and T_1w effects, B_1-inhomogeneitiy and measurement noise.[187–189] The first

validation study for ihMT reported a correlation between ihMTR and PLP green fluorescent protein (GFP) in three mice of $R^2 = 0.87$ to 0.96.[74] As PLP is one of the main proteins within the myelin sheath, this PLP-GFP should show fluorescence distributions similar as quantification with anti-PLP stains or LFB.[69] Almost half of the total ihMT signal is not specific for myelin, which illustrates that the source of ihMT signal is derived from all macromolecules.[74] When filtering the ihMT signal to dipolar order relaxation times T_{1D} related to myelin,[19] correlation with PLP-GFP and LFB is improved, with R^2 values > 0.79, and intercepts are reduced.[69] Further reduction of the intercept is achieved with correction for B_1+ inhomogeneities and R_1 relaxation with the ihMTstat approach,[190,191] resulting in $R^2 > 0.79$ and intercepts close to zero.[69] IhMT is sensitive to tissue orientation[78,192] and its sensitivity to iron is not yet known. In 25 subjects with relapsing-remitting multiple sclerosis, ihMTR (but not MTR) was found to significantly correlate with disability in the thalamus and in four out of five WM regions.[193] In lesions of subjects with relapsing-remitting multiple sclerosis, MTR, qMT and ihMTR all correlated significantly with disability (MTR $R^2 = 0.19$; qMT $R^2 = 0.33$; ihMTR $R^2 = 0.55$; all $P < 0.05$).[165]

Correlations between MWF and myelin staining span a wide range across studies. In the corpus callosum of cuprizone-fed mice and controls an $R^2 = 0.46$ was found,[183] whereas in a study where demyelination was induced by hexachlorophene in rat spinal cord, R^2 was only 0.16.[194] In 25 multiple sclerosis tissue samples from 13 patients at 1.5 T Laule *et al.*[195] determined a mean correlation between LFB optical density and MWF of $R^2 = 0.67$ (ranging from 0.45 to 0.92) when tissues included GM, lesions and WM, and a mean R^2 of 0.29 for WM regions only. In samples from three multiple sclerosis patients at 7 T, the same group found correlation of $R^2 = 0.78$ (range from 0.56 to 0.95) for regions that encompass NAWM, DAWM, GM and lesions, and $R^2 = 0.43$ in WM (range from 0.00–0.79).[196] In a rat spinal cord injury model (12 injured and six controls), using *ex vivo* MRI at 7 T and EM, Chen *et al.*[197] determined a strong correlation of $R^2 = 0.67$ between MWI and EM-determined myelin content, but their study also suggests that MWF does not distinguish between intact myelin and myelin debris.[198] In the same rodent study at 15.2 T described before for MTR, West *et al.*[153] reported an R^2 of 0.66.

In 10 regions of the corpus callosum of 395 healthy individuals (161 males) with ages from 7 to 85 years, MWF showed a quadratic relationship with age and followed a regional pattern, which both agree with histological studies of the corpus callosum.[199–201] A prospective study with pre- and post-injury MRI in ice hockey players showed that MWF is reduced 2 weeks after concussion and recovers by 2 months,[202] in line with animal work in mild traumatic brain injury.[203] For multiple sclerosis, one of the main applications of myelin mapping, the number of MWI studies is small and many of them are from one site. A longitudinal study in 58 patients with multiple sclerosis and 24 controls suggests that ocrelizumab protects against demyelination in all five NAWM regions investigated, and chronic lesions, compared to interferon beta-1a,[204] which is in agreement with ocrelizumab's greater efficacy at preventing disability progression, clinical relapses and new lesions on brain MRI.[205,206] However, across the entire NAWM, no group differences were found, which may be due to MWI's dependence on tissue orientation[32] and regional differences in MWF.[207] In 46 patients with multiple sclerosis, Baumeister *et al.*[208] demonstrated an association between MWF and cognitive performance in multiple sclerosis. Vavasour *et al.*[209] found in 42 multiple sclerosis patients at four sites treated with alemtuzumab that during 24 months after treatment start MWF was stable in lesions (including 50 new lesions) and in NAWM. On the other hand, Abel *et al.*[210] investigated 73 patients with multiple sclerosis and 22 controls and found no association between MWF in any of the regions investigated (cingulum, corpus callosum and superior longitudinal fasciculus) and any of the cognitive tests used.

Unlike MT, MWF usually does go to zero in the absence of myelin.[153] However, studies in rat spinal cord,[211,212] mouse brain[153] and rat optic nerve[212] suggest that exchange effects due to thin myelin sheaths may lead to a reduction in measured MWF, resulting in a small negative intercept. MWF is much less sensitive to changes in water content than MTR.[37] Like many MRI techniques, MWF is sensitive to tissue iron concentration with an MWF reduction of ~25% after chemical iron extraction.[33] Finally, it was demonstrated that MWF depends on the orientation of WM fibres relative to the main magnetic field.[32]

The correlation between QSM (and in earlier literature gradient echo frequency shifts) and myelin histopathology is low in the human brain tissue samples but high in animal studies. In 11 Wistar rats at 9.4 T, the correlation between *in vivo* frequency shifts and myelin staining was $R^2 = 0.67$ in the anterior commissure and $R^2 = 0.76$ in the corpus callosum.[213] A 9.4 T study in 18 *ex vivo* but *in situ* mouse brains at different postnatal ages found a strong correlation between magnetic susceptibility and LFB of $R^2 = 0.93$ and no correlation with iron staining.[214] In eight human tissue samples, Wiggermann *et al.*[215] found no correlation between magnetic susceptibility and myelin, a moderate correlation of $R^2 = 0.33$ between frequency shifts and myelin and no correlation between any MR measures and iron. Reasons for the discrepancy between human tissue samples and animal studies may be the poor field homogeneity in human brain tissue samples and the low iron concentrations in rodent brain compared to humans.[177–179] Iron's paramagnetism has a strong influence on QSM.[216,217] About 8% of multiple sclerosis lesions exhibit an increase in iron, while most lesions show a loss of iron.[149] On a lesion per lesion basis, iron cannot be excluded as a source of increased susceptibility within an multiple sclerosis lesion. At a group level, this uncertainty may be outweighed by QSM's high sensitivity to changes in diamagnetic myelin, which stems from all water being used to probe the resonance frequency. A loss in myelin changes the frequency, but it does not reduce the magnitude of the signal. Moreover, the MR phase, from which QSM is computed, has a considerably higher signal-to-noise ratio (SNR) than the corresponding magnitude.[218,219] However, myelin's magnetic susceptibility itself depends on tissue orientation.[220,221] Nevertheless, QSM is used widely in neuroimaging, mostly owing to its simple and fast data acquisition and the additional information that can be computed from the scan, such as venograms,[222] R_2^* relaxation,[223–225] the visualization of the central vein sign[226] and iron rings around some multiple sclerosis lesions,[227,228] with scan times <5 min at 5 to 20 times higher spatial resolution than any other scan discussed here. Results from QSM have been consistent with brain biology and pathology. For example, analysing 35 885 QSM scans from the UK Biobank study, Wang and colleagues found associations of magnetic susceptibility with genetic variants that encode the myelin protein plasmolipin and the oligodendrocyte basic protein in subregions of the thalamus and widespread WM regions.[229] Scans of neonates, who have almost no myelin or iron show no contrast on QSM, except venous vessels,[230] and regional WM susceptibility in children 0, 1 and >2 years of age correlated strongly with regional myelin content from an earlier autopsy study.[231,232]

The correspondence between the relative semisolid proton fraction from UTE and MBP was $R^2 = 0.27–0.74$ in seven cuprizone-fed and eight control mice at 7 T.[183] In six cuprizone-fed mice (pre-diet,

4 weeks, 6 weeks and 6 weeks + 6 weeks recovery; as well as six mice at each time point for histology with MBP) the R^2 between UTE-MTR at TE = 76 μs and MBP was 0.71.[233] In 10 healthy volunteers and 10 patients with multiple sclerosis, STAIR-UTE differentiated between multiple sclerosis lesions, NAWM and normal WM.[59] UTE requires high RF peak power and strong gradients, as well as a good B_1+ profile.[183] Moreover, gliosis and swelling of astrocyte processes contribute to an increase of non-myelin associated water and therefore affect UTE-MTR and STE-MTR values.[233,234] UTE is also limited by blurring caused by R_2^* relaxation during readout, which is further accelerated at ultra-high field.

Correlation between SyMRI and myelin histology are in the range of $R^2 = 0.37$ to 0.55.[150,235] One study in human post-mortem brain samples of three multiple sclerosis patients found an $R^2 =$ 0.37–0.44 when LFB was used for myelin histology, and an $R^2 =$ 0.40–0.53 when anti-PLP staining was used for myelin histology.[235] Another study assessed the correspondence of SyMRI with myelin histology using post-mortem brain samples of 12 subjects and found an correspondence of $R^2 = 0.55$ using LFB for myelin histology.[150] In addition, a global decrease in myelin density within the brains of multiple sclerosis patients was observed using SyMRI,[236] and SyMRI could detect delayed myelination in preterm neonates and was more sensitive than conventional T_1w and T_2w.[237] Furthermore, myelin imaging with SyMRI demonstrated spatial correspondence myelination in 22 children from 0 to 14 years.[238] However, validation studies are scarce and so far no studies have reported the effects of tissue orientation, iron, B_1 inhomogeneity or changes in water content on SyMRI.

Since PET requires active blood circulation for tracer distribution, it is not possible to conduct histology validation studies in (human) brain tissue *ex vivo*, thus requiring animal studies. In the lysolecithin-induced rat model of demyelination, ^{11}C-MeDAS PET showed a good correlation with post-mortem myelin staining ($R^2 = 0.76$), with tracer uptake expressed as lesion-to-contralateral standardized uptake value ratio.[239] Another study by the same group in the same animal model found a moderate correlation of $R^2 = 0.66$ for ^{11}C-MeDAS, and better correlations of $R^2 = 0.79$ for ^{11}C-PiB and $R^2 = 0.84$ for [^{11}C]CIC, with tracer uptake expressed as the lesion-to-contralateral total volume of distribution ratios.[126] The first human study of ^{11}C-MeDAS PET found the expected range of myelin density from low (black holes) to high (remyelinated lesions) in multiple sclerosis patients.[124] Myelin imaging with PET has been used in multiple sclerosis, where it demonstrated a decrease in myelin density in lesions.[117,118,124,240–243]

For all techniques, correlations across validation studies ranged from weak to strong. The literature discussed before presents mostly the higher end of the range. These studies used well characterized animal models and/or established histology techniques, and therefore best reflect the upper limits of a particular imaging technique. In animal studies, both QSM[213,214] and ihMTR[74] have a high correlation with myelin histopathology ($R^2 = 0.85$ and $R^2 = 0.94$, respectively), followed by *g*-ratio[244] ($R^2 = 0.69$), qMT[153,181–183,194,245–248] ($R^2 =$ 0.60), MWF[147,153,183,194,197] ($R^2 = 0.55$), T_1[176,246] ($R^2 = 0.55$), UTE[183] ($R^2 =$ 0.51), MTR[74,153,176,246,249–254] ($R^2 = 0.42$) and single exponential T_2[153,176,246] ($R^2 = 0.37$). Human post-mortem studies show weak to moderate correlation with myelin histopathology for MWF[195,196] ($R^2 = 0.68$), MTR[143,160–163,255] ($R^2 = 0.65$), qMT[143,161] ($R^2 = 0.60$), SyMRI[150] ($R^2 = 0.55$), T_1[143,160–162,255,256] ($R^2 = 0.48$), T_2[143,162,255,256] ($R^2 = 0.45$), FA[155] ($R^2 = 0.38$), radial diffusivity[155] ($R^2 = 0.34$), MD[155] ($R^2 = 0.26$), AD[155] ($R^2 =$ 0.39), R_2*[142,257] ($R^2 = 0.18$) and QSM[142,215] ($R^2 = 0.07$). The reproducibility of all methods is good to excellent (ICC = 0.75–0.93),[41,46,184,185,258–267] except for MTR (ICC = 0.05–0.51).[46,268]

All the presented MRI techniques are also influenced by effects other than myelin. For example, of the macromolecular content of the CNS, on which UTE and MT are based, only 50% is myelin. ihMT with isolation of the T_{1D} components of myelin macromolecules is emerging as a technique with high specificity. Recent studies identified some putative confounding factors for ihMT that can affect the signal amplitude and thus the signal interpretation. These include sample temperature,[11,77] which is less of a concern *in vivo*, and non-myelin related short-life dipolar order.[78] MWI gains its good specificity from characteristic relaxation times of myelin water, but it suffers from low SNR and direct dependence on reconstructed image intensity. Furthermore, most, if not all, MRI techniques for myelin are sensitive to iron, a strong modifier of magnetic susceptibility and tissue relaxation properties.[33,174,223] At least MWF, MTR, qMT, ihMTR, qihMT, QSM and diffusion-weighted imaging also depend on the angle between anisotropic tissue and the main magnetic field.[32,78,192,269,270] Fitting a tissue model to the orientation-dependent R_2^*, on the other hand, can determine both myelin and iron content, albeit at the cost of loss of spatial information.[223] The local tissue orientation can be measured using DTI.[271] With fast imaging and increased SNR, the trade-off between clinical utility (easy to implement and short scan times) and high specificity becomes less of an issue. Some less-specific techniques remain attractive due to their simplicity, robustness, high sensitivity or short acquisition times.

Clinical applications

Some of the many publications on clinical applications are highlighted before, as their results add to the validation of the respective imaging technique. Among the most important applications of myelin imaging is multiple sclerosis. For multiple sclerosis and demyelinating diseases in general, there is an urgent need for quantitative imaging of myelin for treatment trials.[158] Demyelination in focal lesions is one of the hallmarks of multiple sclerosis.[158,272] New multiple sclerosis lesions with intact axons that have the capacity to remyelinate are considered an important tissue to investigate in clinical trials. Myelin imaging with UTE, MT, *g*-ratio and PET demonstrated a decrease in myelin density in multiple sclerosis lesions.[55,117–119,164,184,241–243,272–274] Magnetic susceptibility-sensitive MRI and MT could detect tissue changes before lesion formation.[275,276] It is not clear whether this indicates early myelin sheath disintegration preceding[277] the inflammatory responses or changes in resonance frequency due to increased chemical exchange effects in the presence of increased blood plasma proteins.[278] As multiple sclerosis pathology extends beyond multiple sclerosis lesions and affects DAWM and NAWM, several studies aimed to assess global myelin integrity in multiple sclerosis, using either SyMRI, MT, QSM or *g*-ratio. These studies found a global decrease in cerebral myelin density.[164,215,236,273–275,279–284] Myelin imaging with MWF, MT, ihMT and *g*-ratio showed that changes in myelin density were associated with disease duration and disability scores in multiple sclerosis.[165,185,193,210] In addition, myelin imaging with ihMT was found to be more sensitive to detect spinal cord damage than MT and diffusion MRI and also correlated better with clinical disability.[165,285]

In mild traumatic brain injury, QSM did not find any change in myelin density in the areas that showed a reduction in myelin signal on MWI post-concussion in the same cohort.[202,286] This finding suggests that the observed change in MWF may not be due to myelin loss, but to decompaction of the myelin sheath as a result of injury, which is in agreement with animal studies of concussion.[203]

Another important application of myelin imaging is brain maturation and brain development. The first brain regions that myelinate postnatally are the primary motor cortex, somatosensory cortex, visual cortex and the auditory cortex,[287] which are subsequently followed by adjacent brain regions.[288,289] Until an age of ~20 years, myelin matures, which is subsequently followed by a decrease of myelin with age.[290,291] With myelin-sensitive imaging methods, these physiological alterations in myelin density across the lifespan have also been observed. For instance, SyMRI could detect delayed myelination in preterm neonates and was more sensitive than conventional MRI methods, such as T_1w and T_2w.[237] Myelin imaging with SyMRI corresponded well with myelination pattern in 22 children from 0 to 14 years.[238] Moreover, a higher myelin density in the corpus callosum, as measured using MWF in children, was strongly correlated with their scores in verbal IQ tests,[292] which indicates that children with a more highly connected corpus callosum might be more verbally developed. Furthermore, in 51 children from 1 to 36 months with a developmental delay, MTR showed a reduced myelin density as compared to healthy controls.[293] In 48 healthy controls with ages ranging from 20 to 70 years, ihMT showed a decrease of myelin with increasing age.[294] In a study on subjects with ages ranging from 21 to 86 years, QSM showed that myelin density was higher in younger adults than in the elderly.[295] Within young children (3 months to 7.5 years), *g*-ratio myelin estimates increased significantly, corresponding with brain maturation.[296] Using the *g*-ratio, a decrease in myelin density with higher age was observed in 102 healthy subjects ranging from 7 to 85 years.[297] However, in another study in 92 healthy subjects from 7 to 81 years, this effect of age was not observed with *g*-ratio.[298] This difference might be due to the myelin imaging technique used, as the former study used MT and the latter PD weighted imaging for calculating *g*-ratio. In general, the MRI methods showed an increase of myelin in early childhood, and a decrease of myelin after early adulthood, in correspondence with physiological processes of myelination in brain development.[299]

Myelin imaging has also been used in other diseases, such as schizophrenia, stroke, isolated hippocampal sclerosis, cognitive dysfunction, neurofibromatosis, Huntington's disease, obsessive-compulsive disorder and major depressive disorder.[300–310]

MRI for myelin is non-invasive and offers a range of complementary image contrasts that can be combined. While, MWF, QSM and ihMT seem to be the most promising MRI methods for myelin imaging from a theoretical perspective, MWF has not yet shown to be able to depict both de- and remyelination processes. One could combine the sensitivity of QSM with the specificity of ihMT, possibly in combination with diffusion MRI, which also enables *g*-ratio imaging. Due to its non-invasiveness, MRI is the only modality that can be used for research in newborns and children. Quantitative MRI has become very fast (2–7 min) and thus the question should not be which myelin scan to use in a study, but which two or three sequences should be combined (Table 2). For example, the combination of a multi-echo gradient echo scan (i.e. SWI/QSM), ihMT and diffusion MRI in multiple sclerosis would provide information on myelin integrity of WM (ihMT); high sensitivity to changes in myelin of lesions, deep GM iron, the central vein sign (QSM); *g*-ratio (combination of MWI and diffusion) and orientation-dependent R_2*[223] for diffuse WM myelin changes (combination of gradient echo and diffusion).[224] This information can all be obtained within a total scan time of 12 to 20 min. Alternatively, one may aim at targeting MWF, myelin macromolecules and magnetic susceptibility using MWI, ihMT and QSM, respectively.

So far, studies with PET for myelin imaging were mostly technical validations.[119,124,126–128,130,131,239,311] The invasiveness of PET due to the administration of a radiotracer and the need for blood sampling, long scan duration, high costs, the complicated quantification procedures and lower availability of PET scans across clinical centres limit the utility of PET for clinical routine. When longitudinal scanning is desired, the clinician should balance the risks of extra radiation exposure with the need for additional PET scans. With further technical developments in PET imaging, the sensitivity and resolution of the PET scans will increase, allowing for lower tracer dose. This would more easily justify the application of PET scans. Nonetheless, the infrastructure needed for PET tracer production makes PET inherently more expensive than MRI. With the introduction of the EARL criteria,[312] PET acquisitions are harmonized. Alternatives for blood sampling exist,[313–315] but require a thorough validation per each individual tracer. From a practical point of view, an accurate myelin MRI method would be preferred above myelin PET. However, myelin imaging with MRI must reach the same accuracy, precision and reproducibility in capturing de- and remyelination as achieved with PET.

Future directions

An important avenue of future research is the validation of techniques such as, VISTA, MR fingerprinting and mcDESPOT. The complex structure of myelin complicates the development of a myelin phantom that can be used for such validation studies. Some research groups make use of phantoms with solubilized myelin proteins, which, however, do not have the structure of alternating lipid bilayers and water.[316] Validation studies in biological tissues should also assess iron content.

Future work should also address the standardization of scan parameters. For example, Birkl *et al.*[32] showed that a scan's TR has a considerable influence on the MWF. The TR effect is thought to be due to the short T_1 relaxation time of myelin water (in the range of 200 ms) compared to that of intra- and extracellular water (1 s).[317] To keep the MWI scan short, usually a repetition time of 1 s is used, which attenuates the long T_1 signal from the intra- and extracellular water. While harmonized scan protocols are used in clinical trials, they are usually not used in other applications. Harmonization efforts should be accompanied by the creation of normative atlases.[207,318,319] Synthetic MRI may further help towards standardization but further work is needed to make it a reliable and validated approach for myelin quantification. There is also a trade-off between harmonization and the speed of technical development.

Field strengths of 7 T and beyond can provide sensitive measurements at high spatial resolution. While clinical 7 T systems are on the market, they still face technical challenges and their cost is high. Over the next decade, these scanners will probably remain limited to specialized centres, such as large academic hospitals. With the exception of gradient echo MRI (SWI/QSM), the translation of myelin imaging techniques to ultra-high field strengths requires considerable technical development. Low-field and ultra-low-field MRI, have made progress due to the development of magnetic resonance fingerprinting, possibly making myelin quantification in dedicated (ultra-) low-field scanners viable in the future.[320,321]

Magnetic resonance fingerprinting provides simultaneous quantification of relaxation properties of the brain in one scan, generating a nearly pseudo-random path through *k*-space.[322–325] The

Table 2 Overview of imaging techniques for which validation studies have been published

Technique	Biophysical origin of contrast	Advantages	Myelin specificity	Sensitivity	Limitations	Acquisition time	Spatial resolution	Software
MWI	Differences in T_2 relaxation times of different water pools (myelin water intra-/extracellular water)	Complementary origin of image contrast to other markers Well defined water pool	Moderate; also sensitive to iron and tissue orientation	Low	High SAR Low SNR Sensitive to post processing parameters	7–12 min	5–8 mm^3	DECAES[37]
UTE	Imaging of the ultra-short T_2 components reveals bound hydrogen in macromolecules	Convenient postprocessing without user interaction available on some scanners Robust to artefacts	Moderate; also sensitive to non-myelin macromolecules	Moderate	High hardware requirements Post processing not standardized	5–10 min		SPM12, FSL, Free surfer[276–278]
MT	Magnetization transfer from bound pool to free water pool	Ease of use, convenient postprocessing without user interaction available on some scanners	Moderate, also sensitive to non-myelin macromolecules	Moderate	Low reproducibility	5–10 min	2.6 mm^3	On scanner
ihMT	Dipolar order of the bound pool	Ease of use, convenient postprocessing without user interaction available on some scanners	High, due to isolation of the myelin dipolar order	Unknown	High hardware requirements	5–10 min	2.6 mm^3	On scanner
SyMRI	Magnetization exchange between myelin water and intra- & extracellular water	Ease of use, convenient post processing in commercial package	Low	Low	Proprietary post processing software	5–10 min	1–25 mm^3	SyMRI[279]
QSM	Magnetic susceptibility of myelin influences R^{2*}	Additionally provides R^{2*} and venous information; very high spatial resolution; high SNR, fast	Moderate; sensitive to iron and tissue orientation	High	Post processing not standardized	~1.5–6 min	0.3–1 mm^3	RTS[99], SEPIA[98]
Diffusion	Diffusion of water in different pools separated by myelin sheets	Virtually universal availability for basic methods, high clinical usability as sequences can be used for multiple indications aside myelin imaging	Low	Medium	High hardware requirements	~3–10 min	Typically 8 mm^3 resolution	MRtrix, FSL[276,280]
PET	Exogenous PET tracers binding to myelin proteins	Absolute quantification	Potentially high; potentially sensitive to other proteins with beta sheath structures	Unknown	Long scan duration, blood sampling; need for isotope production and radiochemistry lab, expensive	20–90 min	2–5 × 2–5 × 2–5 mm^3	PMOD, 3D Slicer[137]

SAR = specific absorption rate; DECAES = Decomposition and component analysis of exponential signals.

k-space data are then matched to a library of simulations of the Bloch–Torrey equations and biophysical models, enabling simultaneous quantification of multiple parameters. This can be thought of as matching fingerprints to unique entries in the library. Most of the MRI contrasts discussed in this article can be translated into a magnetic resonance fingerprinting setting and some have already been used for myelin quantification: T_1 and T_2-quantification,[326] multi-compartment,[327] UTE,[328] diffusion[329] and MT.[330]

Another emerging technique is magnetic resonance elastography, which probes the mechanical properties of tissues[331,332] and has been shown to have a strong test–retest repeatability of 1–7%.[333] The tissue is mechanically excited with a known amplitude and frequency by a transceiver coupled to the tissue or a solid structure around it (e.g. neurocranium), resulting in shear forces in the parenchyma. A phase sensitive pulse sequence with motion encoding gradients is used, yielding the phase that is proportional to the product of the gradient and the mechanical displacement of the tissue[331,333] and can be translated to mechanical tissue parameters.[333,334] Various tissue properties affect the mechanical properties of brain parenchyma in human and murine studies.[335–341] One study found a histopathology verified correlation of tissue stiffness with demyelination in mice.[338] Although the stiffness of multiple sclerosis lesions is similar to healthy tissue,[342] there is a significant reduction in global brain stiffness in multiple sclerosis patients and an increased stiffness in chronic-progressive multiple sclerosis as compared to relapsing-remitting multiple sclerosis.[341]

The spatial resolution of PET has been increasing, due to the reduction of the crystal size in the detectors.[343] In addition, total-body PET systems with improved SNR enable the detection of subtle alterations in tracer uptake simultaneously in the brain and the spinal cord.[344] Direct kinetic modelling during the reconstruction with venous samples for metabolite analysis or population-based metabolites aids in reducing the invasiveness of PET and enhances clinical use.[345,346] With total-body PET, both the heart and aorta are within the field of view, and an image-derived input function to substitute the arterial blood sampling may be used for accurate quantification without arterial blood sampling. Current strategies for image-derived input function in brain PET studies use the carotid arteries for the determination of the blood tracer concentration. The high tracer signal of the PET scan directly after tracer injection is used for carotid delineation. Due to the size of these arteries, a partial volume correction is often required. With PET-MR scanners, MR angiography could be used for an accurate delineation of the carotid arteries, but the partial volume problem persists. Whether arterial blood samples for calibration can be substituted for venous samples or population-based alternatives, also depends on the tracer's properties.

Limitations

There is a vast range of applications of myelin-sensitive MRI in the context of brain development, brain injury and neurological diseases. We limited the discussion of applications herein to myelin imaging methods that were validated with histopathology. For the literature on DTI, we refer to specialized reviews.[101,102,107] We did not address applications in spinal cord to which, in principle, the same considerations apply. However, the spinal cord poses technical challenges due to motion, its small cross section, magnetic susceptibility and CSF flow.[347] We also did not address myelin quantification in the GM. In multiple sclerosis, for example, lesions in the GM play an important role.[123] Even their mere detection with qualitative MRI poses challenges.[348] Spectroscopy is also not addressed in this review. While spectroscopy does not quantify myelin itself, it has the potential to explain biochemical processes associated with de- and remyelination. Moreover, with the advent of ultrafast spectroscopic imaging, the distinction between imaging and spectroscopy could become increasingly academic.[349]

Conclusion

There are a few instances where myelin imaging has provided new insight. For example, it has been used to track changes in myelin across parts of the human lifespan.[350–352] In concussion MWI has shown that there is reduced MWF beyond the time of resolution of clinical symptoms.[202] In multiple sclerosis, fitting a tissue magnetic susceptibility model to R_2^* decay suggested that myelin content is the same in people at risk of multiple sclerosis and healthy controls but that the at-risk group has increased brain iron content.[223] The large UK Biobank study (current $n > 35\,000$ participants) has revealed changes in WM magnetic susceptibility that are associated with genetic variants related to myelin structure and oligodendrocytes.[229] The main aim of myelin imaging remains the tracking of de- and remyelination in patient populations, with the goal to inform treatment decisions and to test new drugs.

MRI and PET offer a range of methods for myelin imaging, with complementary strengths and weaknesses in terms of specificity, sensitivity, spatial resolution, cost and robustness. No scan is perfectly specific to myelin, apart from possibly ^{11}C-MeDAS PET. Among MRI, MWI, ihMT and QSM, including the more recent technique of susceptibility source separation,[353–356] seem to be the most promising methods. These scans target complementary aspects of myelin that can be exploited for quantification. ihMT and MWI have high specificity. However, MWI is not available on all MRI systems. The sensitive QSM is based on the almost universally available high resolution SWI scan, which can also provide information on veins, paramagnetic rims in multiple sclerosis lesions and deep GM iron content, but it requires specialized postprocessing. UTE, MTR and qMT are robust techniques that are sensitive to changes in myelin but they cannot distinguish between myelin and non-myelin macromolecules.

Acknowledgements

We would like to thank Pascalle Mossel for her contributions to some of the figures and Alexander Jaffray for proofreading.

Funding

This work was supported by the Netherlands Organisation for Health Research and Development (ZonMW) with the Dutch MS Research Foundation (Stichting MS Research), grant number PTO-95105010, Canada Research Chairs and Fundação de Amparo à Pesquisa do Estado de São Paulo (FAPESP 2018/15167-1), and partially conducted under the framework of the Departments of Excellence 2018–2022 initiative of the Italian Ministry of Education, University and Research for the Department of Neuroscience, Imaging and Clinical Sciences (DNISC) of the University of Chieti-Pescara, Italy.

Competing interests

The authors report no competing interests.

References

1. Stadelmann C, Timmler S, Barrantes-Freer A, Simons M. Myelin in the central nervous system: Structure, function, and pathology. *Physiol Rev*. 2019;99:1381-1431.
2. Baumann N, Pham-Dinh D. Biology of oligodendrocyte and myelin in the mammalian central nervous system. *Physiol Rev*. 2001;81:871–927.
3. Nave K-A, Werner HB. Myelination of the nervous system: Mechanisms and functions. *Annu Rev Cell Dev Biol*. 2014;30: 503-533.
4. van der Knaap MS, Valk J. Magnetic resonance of myelination and myelin disorders. *Padiatr Prax*. 2006;68:452.
5. Alizadeh A, Dyck SM, Karimi-Abdolrezaee S. Myelin damage and repair in pathologic CNS: Challenges and prospects. *Front Mol Neurosci*. 2015;8:35.
6. Gingele S, Stangel M. Emerging myelin repair agents in preclinical and early clinical development for the treatment of multiple sclerosis. *Expert Opin Investig Drugs*. 2020;29:583-594.
7. Hooijmans CR, Hlavica M, Schuler FAF, *et al*. Remyelination promoting therapies in multiple sclerosis animal models: A systematic review and meta-analysis. *Sci Rep*. 2019;9:1-17.
8. Mackay A, Whittall K, Adler J, Li D, Paty D, Graeb D. *In vivo* visualization of myelin water in brain by magnetic resonance. *Magn Reson Med*. 1994;31:673-677.
9. Varma G, Girard OM, Prevost VH, Grant AK, Duhamel G, Alsop DC. Interpretation of magnetization transfer from inhomogeneously broadened lines (ihMT) in tissues as a dipolar order effect within motion restricted molecules. *J Magn Reson*. 2015; 260:67-76.
10. Campbell JSW, Leppert IR, Narayanan S, *et al*. Promise and pitfalls of g-ratio estimation with MRI. *Neuroimage*. 2018;182:80-96.
11. Swanson SD, Malyarenko DI, Fabiilli ML, Welsh RC, Nielsen J, Srinivasan A. Molecular, dynamic, and structural origin of inhomogeneous magnetization transfer in lipid membranes. *Magn Reson Med*. 2017;77:1318-1328.
12. MacKay AL, Laule C. Magnetic resonance of myelin water: An *in vivo* marker for myelin. *Brain Plast*. 2016;2:71-91.
13. Henkelman RM, Stanisz GJ, Graham SJ. Magnetization transfer in MRI: A review. *NMR Biomed*. 2001;14:57-64.
14. Varma G, Girard OM, Prevost VH, Grant AK, Duhamel G, Alsop DC. In vivo measurement of a new source of contrast, the dipolar relaxation time, T_{1D}, using a modified inhomogeneous magnetization transfer (ihMT) sequence. *Magn Reson Med*. 2017;78:1362-1372.
15. Vaidman L. Torque and force on a magnetic dipole. *Am J Phys*. 1990;58:978-983.
16. Bloembergen N, Purcell EM, Pound RV. Relaxation effects in nuclear magnetic resonance absorption. *Phys Rev*. 1948;73:679-712.
17. Bloembergen N. Spin relaxation processes in a two-proton system. *Phys Rev*. 1956;104:1542-1547.
18. Solomon I. Relaxation processes in a system of two spins. *Phys Rev*. 1955;99:559.
19. Carvalho VND, Hertanu A, Grélard A, *et al*. MRI Assessment of multiple dipolar relaxation time (T_1D) components in biological tissues interpreted with a generalized inhomogeneous magnetization transfer (ihMT) model. *J Magn Reson*. 2020;311:106668.
20. Goldman M. Formal theory of spin–lattice relaxation. *J Magn Reson*. 2001;149:160-187.
21. Warntjes M, Engström M, Tisell A, Lundberg P. Modeling the presence of myelin and edema in the brain based on multiparametric quantitative MRI. *Front Neurol*. 2016;7:16.
22. Deoni SCL, Rutt BK, Arun T, Pierpaoli C, Jones DK. Gleaning multicomponent T_1 and T_2 information from steady-state imaging data. *Magn Reson Med*. 2008;60:1372-1387.
23. Varma G, Duhamel G, de Bazelaire C, Alsop DC. Magnetization transfer from inhomogeneously broadened lines: A potential marker for myelin. *Magn Reson Med*. 2015;73:614-622.
24. Menon RS, Rusinko MS, Allen PS. Multiexponential proton relaxation in model cellular systems. *Magn Reson Med*. 1991;20:196-213.
25. Whittall KP, MacKay AL, Graeb DA, Nugent RA, Li DK, Paty DW. *In vivo* measurement of T_2 distributions and water contents in normal human brain. *Magn Reson Med*. 1997;37:34-43.
26. Prasloski T, Rauscher A, MacKay AL, *et al*. Rapid whole cerebrum myelin water imaging using a 3D GRASE sequence. *Neuroimage*. 2012;63:533-539.
27. Lustig M, Donoho D, Pauly JM. Sparse MRI: The application of compressed sensing for rapid MR imaging. *Magn Reson Med*. 2007;58:1182-1195.
28. Dvorak AV, Wiggermann V, Gilbert G, *et al*. Multi-spin echo T_2 relaxation imaging with compressed sensing (METRICS) for rapid myelin water imaging. *Magn Reson Med*. 2020;84:1264-1279.
29. Wiggermann V, MacKay AL, Rauscher A, Helms G. *In vivo* investigation of the multi-exponential T_2 decay in human white matter at 7 T: Implications for myelin water imaging at UHF. *NMR Biomed*. 2021;34:e4429.
30. Lenz C, Klarhöfer M, Scheffler K. Feasibility of *in vivo* myelin water imaging using 3D multigradient-echo pulse sequences. *Magn Reson Med*. 2012;68:523-528.
31. Whittall KP, MacKay AL. Quantitative interpretation of NMR relaxation data. *J Magn Reson*. 1989;84:134-152.
32. Birkl C, Doucette J, Fan M, Hernández-Torres E, Rauscher A. Myelin water imaging depends on white matter fiber orientation in the human brain. *Magn Reson Med*. 2021;85:2221-2231.
33. Birkl C, Birkl-Toeglhofer AM, Endmayr V, *et al*. The influence of brain iron on myelin water imaging. *Neuroimage*. 2019;199:545-552.
34. Prasloski T, Mädler B, Xiang QS, MacKay A, Jones C. Applications of stimulated echo correction to multicomponent T_2 analysis. *Magn Reson Med*. 2012;67:1803-1814.
35. Hennig J. Multiecho imaging sequences with low refocusing flip angles. *J Magn Reson*. 1988;78:397-407.
36. Doucette J, Kames C, Rauscher A. DECAES - Decomposition and component analysis of exponential signals. *Z Med Phys*. 2020; 30:271-278.
37. Vavasour IM, Chang KL, Combes AJE, *et al*. Water content changes in new multiple sclerosis lesions have a minimal effect on the determination of myelin water fraction values. *J Neuroimaging*. 2021;31:1119-1125.
38. Sabouri S, Chang SD, Goldenberg SL, *et al*. Comparing diagnostic accuracy of luminal water imaging with diffusion-weighted and dynamic contrast-enhanced MRI in prostate cancer: A quantitative MRI study. *NMR Biomed*. 2019;32:e4048.
39. Sabouri S, Chang SD, Savdie R, *et al*. Luminal water imaging: A new MR imaging T_2 mapping technique for prostate cancer diagnosis. *Radiology*. 2017;284:451-459.
40. Warntjes JBM, Leinhard OD, West J, Lundberg P. Rapid magnetic resonance quantification on the brain: Optimization for clinical usage. *Magn Reson Med*. 2008;60:320-329.
41. Fujita S, Hagiwara A, Hori M, *et al*. Three-dimensional high-resolution simultaneous quantitative mapping of the whole brain with 3D-QALAS: An accuracy and repeatability study. *Magn Reson Imaging*. 2019;63:235-243.
42. Horch RA, Gochberg DF, Nyman JS, Does MD. Clinically compatible MRI strategies for discriminating bound and pore water in cortical bone. *Magn Reson Med*. 2012;68:1774-1784.
43. Boucneau T, Cao P, Tang S, *et al*. *In vivo* characterization of brain ultrashort-T_2 components. *Magn Reson Med*. 2018;80:726-735.
44. Waldman A, Rees JH, Brock CS, Robson MD, Gatehouse PD, Bydder GM. MRI of the brain with ultra-short echo-time pulse sequences. *Neuroradiology*. 2003;45:887-892.

45. Du J, Ma G, Li S, *et al*. Ultrashort echo time (UTE) magnetic resonance imaging of the short T_2 components in white matter of the brain using a clinical 3T scanner. *Neuroimage*. 2014;87:32-41.
46. van der Weijden CWJ, García DV, Borra RJH, *et al*. Myelin quantification with MRI: A systematic review of accuracy and reproducibility. *Neuroimage*. 2021;226:117561.
47. Glasser MF, Van Essen DC. Mapping human cortical areas in vivo based on myelin content as revealed by T_1-and T_2-weighted MRI. *J Neurosci*. 2011;31:11597-11616.
48. Uddin MN, Figley TD, Marrie RA, Figley CR. Can T_1w/T_2w ratio be used as a myelin-specific measure in subcortical structures? Comparisons between FSE-based T_1w/T_2w ratios, GRASE-based T_1w/T_2w ratios and multi-echo GRASE-based myelin water fractions. *NMR Biomed*. 2018;31:e3868.
49. Uddin MN, Figley TD, Solar KG, Shatil AS, Figley CR. Comparisons between multi-component myelin water fraction, T_1w/T_2w ratio, and diffusion tensor imaging measures in healthy human brain structures. *Sci Rep*. 2019;9:2500.
50. West DJ, Teixeira RPAG, Wood TC, Hajnal JV, Tournier J-D, Malik SJ. Inherent and unpredictable bias in multi-component DESPOT myelin water fraction estimation. *Neuroimage*. 2019; 195:78-88.
51. Bernstein MA, King KF, Zhou XJ. *Handbook of MRI pulse sequences*. Amsterdam: Elsevier; 2004.
52. Oh S-H, Bilello M, Schindler M, Markowitz CE, Detre JA, Lee J. Direct visualization of short transverse relaxation time component (ViSTa). *Neuroimage*. 2013;83:485-492.
53. Choi JY, Jeong IH, Oh S-H, *et al*. Evaluation of normal-appearing white matter in multiple sclerosis using direct visualization of short transverse relaxation time component (ViSTa) myelin water imaging and gradient echo and spin echo (GRASE) myelin water imaging. *J Magn Reson Imaging*. 2019;49:1091-1098.
54. Torrey HC. Bloch equations with diffusion terms. *Phys Rev*. 1956;104:563.
55. Sheth V, Shao H, Chen J, *et al*. Magnetic resonance imaging of myelin using ultrashort echo time (UTE) pulse sequences: Phantom, specimen, volunteer and multiple sclerosis patient studies. *Neuroimage*. 2016;136:37-44.
56. Bernstein MA, King KF, Zhou XJ. Chapter 6 - Adiabatic radiofrequency pulses. In: *Handbook of MRI pulse sequences*: Elsevier; 2004:177-212. https://doi.org/10.1016/B978-012092861-3/50010-8
57. Suzuki S, Sakai O, Jara H. Combined volumetric T_1, T_2 and secular-T_2 quantitative MRI of the brain: Age-related global changes (preliminary results). *Magn Reson Imaging*. 2006;24: 877-887.
58. Cheng H-LM, Stikov N, Ghugre NR, Wright GA. Practical medical applications of quantitative MR relaxometry. *J Magn Reson Imaging*. 2012;36:805-824.
59. Ma Y-J, Jang H, Wei Z, *et al*. Myelin imaging in human brain using a short repetition time adiabatic inversion recovery prepared ultrashort echo time (STAIR-UTE) MRI sequence in multiple sclerosis. *Radiology*. 2020;297:392.
60. Ma Y-J, Searleman AC, Jang H, *et al*. Whole-brain myelin imaging using 3D double-echo sliding inversion recovery ultrashort echo time (DESIRE UTE) MRI. *Radiology*. 2020;294:362-374.
61. Port JD. Why we DESIRE to directly image brain myelin using MRI. *Radiology*. 2020;294:375-376.
62. Jang H, Ma Y-J, Chang EY, *et al*. Inversion recovery ultrashort TE MR imaging of myelin is significantly correlated with disability in patients with multiple sclerosis. *AJNR Am J Neuroradiol*. 2021; 42:868-874.
63. Ma Y, Searleman AC, Jang H, *et al*. Volumetric imaging of myelin *in vivo* using 3D inversion recovery-prepared ultrashort echo time cones magnetic resonance imaging. *NMR Biomed*. 2020;33:e4326.
64. Morrison C, Mark Henkelman R. A model for magnetization transfer in tissues. *Magn Reson Med*. 1995;33:475-482.
65. Cercignani M. MT: Magnetisation transfer 1. In: Cercignani M, Dowell NG, Tofts PS, eds. *Quantitative MRI of the brain: Principles of physical measurement*. CRC Press; 2018:161-184.
66. Ulmer JL, Mathews VP, Hamilton CA, Elster AD, Moran PR. Magnetization transfer or spin-lock? An investigation of off-resonance saturation pulse imaging with varying frequency offsets. *Am J Neuroradiol*. 1996;17:805-819.
67. Sled JG, Pike GB. Quantitative interpretation of magnetization transfer in spoiled gradient echo MRI sequences. *J Magn Reson*. 2000;145:24-36.
68. Yarnykh VL. Fast macromolecular proton fraction mapping from a single off-resonance magnetization transfer measurement. *Magn Reson Med*. 2012;68:166-178.
69. Hertanu A, Soustelle L, Buron J, *et al*. T_{1D}-weighted ihMT imaging–part II. Investigating the long-and short-T_{1D} components correlation with myelin content. Comparison with R_1 and the macromolecular proton fraction. *Magn Reson Med*. 2022;87:2329-2346.
70. Provotorov BN. Magnetic resonance saturation in crystals. *Sov Phys JETP*. 1962;14:1126-1131.
71. Manning AP, Chang KL, MacKay AL, Michal CA. The physical mechanism of "inhomogeneous" magnetization transfer MRI. *J Magn Reson*. 2017;274:125-136.
72. Girard OM, Prevost VH, Varma G, Cozzone PJ, Alsop DC, Duhamel G. Magnetization transfer from inhomogeneously broadened lines (ihMT): Experimental optimization of saturation parameters for human brain imaging at 1.5 tesla. *Magn Reson Med*. 2015;73:2111-2121.
73. Morrison C, Stanisz G, Henkelman RM. Modeling magnetization transfer for biological-like systems using a semi-solid pool with a super-Lorentzian lineshape and dipolar reservoir. *J Magn Reson Ser B*. 1995;108:103-113.
74. Duhamel G, Prevost VH, Cayre M, *et al*. Validating the sensitivity of inhomogeneous magnetization transfer (ihMT) MRI to myelin with fluorescence microscopy. *Neuroimage*. 2019;199:289-303.
75. Geeraert BL, Lebel RM, Mah AC, *et al*. A comparison of inhomogeneous magnetization transfer, myelin volume fraction, and diffusion tensor imaging measures in healthy children. *Neuroimage*. 2018;182:343-350.
76. Prevost VH, Girard OM, Varma G, Alsop DC, Duhamel G. Minimizing the effects of magnetization transfer asymmetry on inhomogeneous magnetization transfer (ihMT) at ultra-high magnetic field (11.75 T). *MAGMA*. 2016;29:699-709.
77. Prevost VH, Yung A, Morris SR, *et al*. Temperature dependence and histological correlation of inhomogeneous magnetization transfer and myelin water imaging in *ex vivo* brain. *Neuroimage*. 2021;236:118046.
78. Prevost VH, Girard OM, Mchinda S, Varma G, Alsop DC, Duhamel G. Optimization of inhomogeneous magnetization transfer (ihMT) MRI contrast for preclinical studies using dipolar relaxation time (T_{1D}) filtering. *NMR Biomed*. 2017;30:e3706.
79. Liu C, Li W, Tong KA, Yeom KW, Kuzminski S. Susceptibility-weighted imaging and quantitative susceptibility mapping in the brain. *J Magn Reson imaging*. 2015;42:23-41.
80. Rauscher A, Sedlacik J, Deistung A, Mentzel H-J, Reichenbach JR. Susceptibility weighted imaging: Data acquisition, image reconstruction and clinical applications. *Z Med Phys*. 2006;16: 240-250.
81. Shmueli K, de Zwart JA, van Gelderen P, Li T, Dodd SJ, Duyn JH. Magnetic susceptibility mapping of brain tissue *in vivo* using MRI phase data. *Magn Reson Med*. 2009;62:1510-1522.
82. Deistung A, Schweser F, Reichenbach JR. Overview of quantitative susceptibility mapping. *NMR Biomed*. 2017;30:e3569.

83. Liu C, Li W, Johnson GA, Wu B. High-field (9.4 T) MRI of brain dysmyelination by quantitative mapping of magnetic susceptibility. *Neuroimage*. 2011;56:930-938.
84. Wang N, Zhuang J, Wei H, Dibb R, Qi Y, Liu C. Probing demyelination and remyelination of the cuprizone mouse model using multimodality MRI. *J Magn Reson Imaging*. 2019;50:1852-1865.
85. Lee J, Shmueli K, Kang B-T, *et al*. The contribution of myelin to magnetic susceptibility-weighted contrasts in high-field MRI of the brain. *Neuroimage*. 2012;59:3967-3975.
86. Denk C, Rauscher A. Susceptibility weighted imaging with multiple echoes. *J Magn Reson Imaging*. 2010;31:185-191.
87. Berg RC, Preibisch C, Thomas DL, Shmueli K, Biondetti E. Investigating the effect of flow compensation and quantitative susceptibility mapping method on the accuracy of venous susceptibility measurement. *Neuroimage*. 2021;240:118399.
88. Kames C, Doucette J, Birkl C, Rauscher A. Recovering SWI-filtered phase data using deep learning. *Magn Reson Med*. 2022;87:948-959.
89. Liu T, Wisnieff C, Lou M, Chen W, Spincemaille P, Wang Y. Nonlinear formulation of the magnetic field to source relationship for robust quantitative susceptibility mapping. *Magn Reson Med*. 2013;69:467-476.
90. Chan K-S, Marques JP. SEPIA—Susceptibility mapping pipeline tool for phase images. *Neuroimage*. 2021;227:117611.
91. Kames C, Wiggermann V, Rauscher A. Rapid two-step dipole inversion for susceptibility mapping with sparsity priors. *Neuroimage*. 2018;167:276-283.
92. Basser PJ, Mattiello J, LeBihan D. MR diffusion tensor spectroscopy and imaging. *Biophys J*. 1994;66:259-267.
93. Basser PJ, Mattiello J, LeBihan D. Estimation of the effective self-diffusion tensor from the NMR spin echo. *J Magn Reson B*. 1994;103:247-254.
94. Alexander AL, Lee JE, Lazar M, Field AS. Diffusion tensor imaging of the brain. *Neurother J Am Soc Exp Neurother*. 2007;4:316-329.
95. Beaulieu C, Allen PS. Water diffusion in the giant axon of the squid: Implications for diffusion-weighted MRI of the nervous system. *Magn Reson Med*. 1994;32:579-583.
96. Beaulieu C, Allen PS. Determinants of anisotropic water diffusion in nerves. *Magn Reson Med*. 1994;31:394-400.
97. Le Bihan D, Iima M. Diffusion magnetic resonance imaging: What water tells us about biological tissues. *PLoS Biol*. 2015;13:e1002203.
98. Le Bihan D, Turner R, Douek P, Patronas N. Diffusion MR imaging: Clinical applications. *AJR Am J Roentgenol*. 1992;159:591-599.
99. Larsson HB, Thomsen C, Frederiksen J, Stubgaard M, Henriksen O. *In vivo* magnetic resonance diffusion measurement in the brain of patients with multiple sclerosis. *Magn Reson Imaging*. 1992;10:7-12.
100. Mädler B, Drabycz SA, Kolind SH, Whittall KP, MacKay AL. Is diffusion anisotropy an accurate monitor of myelination? Correlation of multicomponent T_2 relaxation and diffusion tensor anisotropy in human brain. *Magn Reson Imaging*. 2008;26:874-888.
101. Le Bihan D, Mangin JF, Poupon C, *et al*. Diffusion tensor imaging: Concepts and applications. *J Magn Reson Imaging*. 2001;13:534-546.
102. Huston JM, Field AS. Clinical applications of diffusion tensor imaging. *Magn Reson Imaging Clin N Am*. 2013;21:279-298.
103. Zhang H, Schneider T, Wheeler-Kingshott CA, Alexander DC. NODDI: Practical *in vivo* neurite orientation dispersion and density imaging of the human brain. *Neuroimage*. 2012;61:1000-1016.
104. de Kouchkovsky I, Fieremans E, Fleysher L, Herbert J, Grossman RI, Inglese M. Quantification of normal-appearing white matter tract integrity in multiple sclerosis: A diffusion kurtosis imaging study. *J Neurol*. 2016;263:1146-1155.
105. Wang Y, Wang Q, Haldar JP, *et al*. Quantification of increased cellularity during inflammatory demyelination. *Brain*. 2011;134(Pt 12):3590-3601.
106. Schiavi S, Petracca M, Sun P, *et al*. Non-invasive quantification of inflammation, axonal and myelin injury in multiple sclerosis. *Brain*. 2021;144:213-223.
107. Novikov DS, Fieremans E, Jespersen SN, Kiselev VG. Quantifying brain microstructure with diffusion MRI: Theory and parameter estimation. *NMR Biomed*. 2019;32:e3998.
108. Mohammadi S, Callaghan MF. Towards *in vivo g*-ratio mapping using MRI: Unifying myelin and diffusion imaging. *J Neurosci Methods*. 2021;348:108990.
109. Stikov N, Campbell JSW, Stroh T, *et al*. *In vivo* histology of the myelin *g*-ratio with magnetic resonance imaging. *Neuroimage*. 2015;118:397-405.
110. Chomiak T, Hu B. What is the optimal value of the *g*-ratio for myelinated fibers in the rat CNS? A theoretical approach. *PLoS ONE*. 2009;4:e7754.
111. Mohammadi S, Carey D, Dick F, *et al*. Whole-brain *in-vivo* measurements of the axonal G-ratio in a group of 37 healthy volunteers. *Front Neurosci*. 2015;9:441.
112. Melbourne A, Toussaint N, Owen D, *et al*. Niftyfit: A software package for multi-parametric model-fitting of 4D magnetic resonance imaging data. *Neuroinformatics*. 2016;14:319-337.
113. Bailey DL, Townsend DW, Valk PE. *Positron Emission Tomography: Basic Sciences*. Berlin: Springer; 2005.
114. Berger A. Positron emission tomography. *Br Med J*. 2003;326:1449.
115. Ridsdale RA, Beniac DR, Tompkins TA, Moscarello MA, Harauz G. Three-dimensional structure of myelin basic protein. *J Biol Chem*. 1997;272:4269–4275.
116. van der Weijden CWJ, Meilof JF, de Vries EFJ. PET imaging in multiple sclerosis. In: Dierckx RAJO, Otte A, de Vries EFJ, van Waarde A, Leenders KL, eds. *PET And SPECT in neurology*. Springer International Publishing; 2021:893-916. doi:10.1007/978-3-030-53168-3_33
117. Zeydan B, Lowe VJ, Schwarz CG, *et al*. Pittsburgh compound-B PET white matter imaging and cognitive function in late multiple sclerosis. *Mult Scler J*. 2018;24:739-749.
118. Matías-Guiu JA, Cabrera-Martín MN, Matías-Guiu J, *et al*. Amyloid PET imaging in multiple sclerosis: An 18F-florbetaben study. *BMC Neurol*. 2015;15:1-7.
119. Bodini B, Veronese M, García-Lorenzo D, *et al*. Dynamic imaging of individual remyelination profiles in multiple sclerosis. *Ann Neurol*. 2016;79:726–738.
120. Wu C, Bowers MT, Shea JE. On the origin of the stronger binding of PIB over thioflavin T to protofibrils of the Alzheimer amyloid-β peptide: A molecular dynamics study. *Biophys J*. 2011;100:1316–1324.
121. Dal Bianco A, Bradl M, Frischer J, Kutzelnigg A, Jellinger K, Lassmann H. Multiple sclerosis and Alzheimer's disease. *Ann Neurol*. 2008;63:174-183.
122. de Paula Faria D. Myelin positron emission tomography (PET) imaging in multiple sclerosis. *Neural Regen Res*. 2020;15:1842-1843.
123. Kutzelnigg A, Lucchinetti CF, Stadelmann C, *et al*. Cortical demyelination and diffuse white matter injury in multiple sclerosis. *Brain*. 2005;128(Pt 11):2705-2712.
124. van der Weijden CWJ, Meilof JF, van der Hoorn A, *et al*. Quantitative assessment of myelin density using [^{11}C]MeDAS PET in patients with multiple sclerosis: A first-in-human study. *Eur J Nucl Med Mol Imaging*. 2022;49:3492–3507.
125. Luczynski P, Laule C, Hsiung G-YR, Moore GRW, Tremlett H. Coexistence of multiple sclerosis and Alzheimer's disease: A review. *Mult Scler Relat Disord*. 2019;27:232-238.

126. De Paula Faria D, Copray S, Sijbesma JWA, *et al*. PET Imaging of focal demyelination and remyelination in a rat model of multiple sclerosis: Comparison of [^{11}C]MeDAS, [^{11}C]CIC and [^{11}C] PIB. *Eur J Nucl Med Mol Imaging*. 2014;41:995-1003.
127. de Paula Faria D, De Vries EFJ, Sijbesma JWA, Dierckx RAJO, Buchpiguel CA, Copray S. PET Imaging of demyelination and remyelination in the cuprizone mouse model for multiple sclerosis: A comparison between [^{11}C]CIC and [^{11}C]MeDAS. *Neuroimage*. 2014;87:395-402.
128. Wu C, Wei J, Tian D, Feng Y, Miller RH, Wang Y. Molecular probes for imaging myelinated white matter in CNS. *J Med Chem*. 2008;51:6682-6688.
129. Stankoff B, Wang Y, Bottlaender M, *et al*. Imaging of CNS myelin by positron-emission tomography. *Proc Natl Acad Sci USA*. 2006;103:9304-9309.
130. Wu C, Zhu J, Baeslack J, *et al*. Longitudinal positron emission tomography imaging for monitoring myelin repair in the spinal cord. *Ann Neurol*. 2013;74:688-698.
131. Wu C, Wang C, Popescu DC, *et al*. A novel PET marker for *in vivo* quantification of myelination. *Bioorganic Med Chem*. 2010;18: 8592-8599.
132. Brugarolas P, Sánchez-Rodríguez JE, Tsai H-M, *et al*. Development of a PET radioligand for potassium channels to image CNS demyelination. *Sci Rep*. 2018;8:607.
133. Guehl NJ, Ramos-Torres KM, Linnman C, *et al*. Evaluation of the potassium channel tracer [^{18}F] 3F4AP in rhesus macaques. *J Cereb Blood Flow Metab*. 2021;41:1721-1733.
134. Carson RE. Tracer kinetic modeling in PET. In: Bailey DL, Townsend DW, Valk PE, Maisey MN, eds. *Positron emission tomography*: Springer; 2005:127-159.
135. Panin VY, Bal H, Defrise M, Casey ME, Karakatsanis NA, Rahmim A. Whole body parametric imaging on clinical scanner: Direct 4D reconstruction with simultaneous attenuation estimation and time-dependent normalization. In: *2015 IEEE nuclear science symposium and medical imaging conference (NSS/MIC)*. IEEE; 2015:1-7.
136. Meikle SR, Matthews JC, Cunningham VJ, *et al*. Parametric image reconstruction using spectral analysis of PET projection data. *Phys Med Biol*. 1998;43:651.
137. Fedorov A, Beichel R, Kalpathy-Cramer J, *et al*. 3D slicer as an image computing platform for the quantitative imaging network. *Magn Reson Imaging*. 2012;30:1323-1341.
138. Seifert AC, Umphlett M, Hefti M, Fowkes M, Xu J. Formalin tissue fixation biases myelin-sensitive MRI. *Magn Reson Med*. 2019;82:1504-1517.
139. Birkl C, Soellradl M, Toeglhofer AM, *et al*. Effects of concentration and vendor specific composition of formalin on postmortem MRI of the human brain. *Magn Reson Med*. 2018;79: 1111-1115.
140. Birkl C, Langkammer C, Golob-Schwarzl N, *et al*. Effects of formalin fixation and temperature on MR relaxation times in the human brain. *NMR Biomed*. 2016;29:458-465.
141. Wang C, Song L, Zhang R, Gao F. Impact of fixation, coil, and number of excitations on diffusion tensor imaging of rat brains at 7.0 T. *Eur Radiol Exp*. 2018;2:25.
142. Hametner S, Endmayr V, Deistung A, *et al*. The influence of brain iron and myelin on magnetic susceptibility and effective transverse relaxation—A biochemical and histological validation study. *Neuroimage*. 2018;179:117-133.
143. Schmierer K, Wheeler-Kingshott CAM, Tozer DJ, *et al*. Quantitative magnetic resonance of postmortem multiple sclerosis brain before and after fixation. *Magn Reson Med*. 2008;59:268-277.
144. Fishbein KW, Gluzband YA, Kaku M, *et al*. Effects of formalin fixation and collagen cross-linking on T_2 and magnetization transfer in bovine nasal cartilage. *Magn Reson Med*. 2007;57: 1000-1011.
145. Fox CH, Johnson FB, Whiting J, Roller PP. Formaldehyde fixation. *J Histochem Cytochem*. 1985;33:845-853.
146. Kamman RL, Go KG, Stomp GP, Hulstaert CE, Berendsen HJC. Changes of relaxation times T_1 and T_2 in rat tissues after biopsy and fixation. *Magn Reson Imaging*. 1985;3:245-250.
147. Kozlowski P, Raj D, Liu J, Lam C, Yung AC, Tetzlaff W. Characterizing white matter damage in rat spinal cord with quantitative MRI and histology. *J Neurotrauma*. 2008;25: 653-676.
148. Kiernan JA. Histochemistry of staining methods for normal and degenerating myelin in the central and peripheral nervous systems. *J Histotechnol*. 2007;30:87-106.
149. Hametner S, Wimmer I, Haider L, Pfeifenbring S, Brück W, Lassmann H. Iron and neurodegeneration in the multiple sclerosis brain. *Ann Neurol*. 2013;74:848-861.
150. Warntjes JBM, Persson A, Berge J, Zech W. Myelin detection using rapid quantitative MR imaging correlated to macroscopically registered luxol fast blue-stained brain specimens. *Am J Neuroradiol*. 2017;38:1096-1102.
151. Tang Y, Nyengaard JR. A stereological method for estimating the total length and size of myelin fibers in human brain white matter. *J Neurosci Methods*. 1997;73:193-200.
152. Denef J-F, Cordier AC, Mesquita M, Haumont S. The influence of fixation procedure, embedding medium and section thickness on morphometric data in thyroid gland. *Histochemistry*. 1979;63:163-171.
153. West KL, Kelm ND, Carson RP, Gochberg DF, Ess KC, Does MD. Myelin volume fraction imaging with MRI. *Neuroimage*. 2018; 182:511-521.
154. Piredda GF, Hilbert T, Thiran J-P, Kober T. Probing myelin content of the human brain with MRI: A review. *Magn Reson Med*. 2021;85:627-652.
155. Mancini M, Karakuzu A, Cohen-Adad J, Cercignani M, Nichols TE, Stikov N. An interactive meta-analysis of MRI biomarkers of myelin. *eLife*. 2020;9:e61523.
156. Lazari A, Lipp I. Can MRI measure myelin? Systematic review, qualitative assessment, and meta-analysis of studies validating microstructural imaging with myelin histology. *Neuroimage*. 2021;230:117744.
157. York EN, Thrippleton MJ, Meijboom R, Hunt DPJ, Waldman AD. Quantitative magnetization transfer imaging in relapsing-remitting multiple sclerosis: A systematic review and meta-analysis. *Brain Commun*. 2022;4:fcac088.
158. Oh J, Ontaneda D, Azevedo C, *et al*. Imaging outcome measures of neuroprotection and repair in MS: A consensus statement from NAIMS. *Neurology*. 2019;92:519-533.
159. Beckmann N, Giorgetti E, Neuhaus A, *et al*. Brain region-specific enhancement of remyelination and prevention of demyelination by the CSF1R kinase inhibitor BLZ945. *Acta Neuropathol Commun*. 2018;6:1-17.
160. Schmierer K, Scaravilli F, Altmann DR, Barker GJ, Miller DH. Magnetization transfer ratio and myelin in postmortem multiple sclerosis brain. *Ann Neurol*. 2004;56:407-415.
161. Schmierer K, Tozer DJ, Scaravilli F, *et al*. Quantitative magnetization transfer imaging in postmortem multiple sclerosis brain. *J Magn Reson Imaging*. 2007;26:41-51.
162. Mottershead JP, Schmierer K, Clemence M, *et al*. High field MRI correlates of myelin content and axonal density in multiple sclerosis: A post-mortem study of the spinal cord. *J Neurol*. 2003;250:1293-1301.
163. Van Der Voorn JP, Pouwels PJW, Powers JM, *et al*. Correlating quantitative MR imaging with histopathology in X-linked adrenoleukodystrophy. *Am J Neuroradiol*. 2011;32:481-489.

164. Newbould RD, Nicholas R, Thomas CL, *et al*. Age independently affects myelin integrity as detected by magnetization transfer magnetic resonance imaging in multiple sclerosis. *NeuroImage Clin*. 2014;4:641-648.
165. Zhang L, Wen B, Chen T, *et al*. A comparison study of inhomogeneous magnetization transfer (ihMT) and magnetization transfer (MT) in multiple sclerosis based on whole brain acquisition at 3.0 T. *Magn Reson Imaging*. 2020;70:43-49.
166. Button T, Altmann D, Tozer D, *et al*. Magnetization transfer imaging in multiple sclerosis treated with alemtuzumab. *Mult Scler*. 2013;19:241-244.
167. Moccia M, van de Pavert S, Eshaghi A, *et al*. Pathologic correlates of the magnetization transfer ratio in multiple sclerosis. *Neurology*. 2020;95:e2965-e2976.
168. Does MD, Beaulieu C, Allen PS, Snyder RE. Multi-component T_1 relaxation and magnetisation transfer in peripheral nerve. *Magn Reson Imaging*. 1998;16:1033-1041.
169. Dousset V, Grossman RI, Ramer KN, *et al*. Experimental allergic encephalomyelitis and multiple sclerosis: Lesion characterization with magnetization transfer imaging. *Radiology*. 1992;182:483-491.
170. Gareau PJ, Rutt BK, Karlik SJ, Mitchell JR. Magnetization transfer and multicomponent T_2 relaxation measurements with histopathologic correlation in an experimental model of MS. *J Magn Reson Imaging*. 2000;11:586-595.
171. Vavasour IM, Laule C, Li DKB, Traboulsee AL, MacKay AL. Is the magnetization transfer ratio a marker for myelin in multiple sclerosis? *J Magn Reson Imaging*. 2011;33:710-718.
172. Stanisz GJ, Odrobina EE, Pun J, *et al*. T_1, T_2 relaxation and magnetization transfer in tissue at 3T. *Magn Reson Med*. 2005;54:507-512.
173. Serres S, Anthony DC, Jiang Y, *et al*. Comparison of MRI signatures in pattern I and II multiple sclerosis models. *NMR Biomed*. 2009;22:1014-1024.
174. Birkl C, Birkl-Toeglhofer AM, Kames C, *et al*. The influence of iron oxidation state on quantitative MRI parameters in post mortem human brain. *Neuroimage*. 2020;220:117080.
175. Langkammer C, Krebs N, Goessler W, *et al*. Susceptibility induced gray–white matter MRI contrast in the human brain. *Neuroimage*. 2012;59:1413-1419.
176. Hakkarainen H, Sierra A, Mangia S, *et al*. MRI relaxation in the presence of fictitious fields correlates with myelin content in normal rat brain. *Magn Reson Med*. 2016;75:161-168.
177. Hallgren B, Sourander P. The effect of age on the non-haemin iron in the human brain. *J Neurochem*. 1958;3:41-51.
178. Pal A, Prasad R. Regional distribution of copper, zinc and iron in brain of wistar rat model for non-Wilsonian brain copper toxicosis. *Indian J Clin Biochem*. 2016;31:93-98.
179. Desmond KL, Al-Ebraheem A, Janik R, *et al*. Differences in iron and manganese concentration may confound the measurement of myelin from R_1 and R_2 relaxation rates in studies of dysmyelination. *NMR Biomed*. 2016;29:985-998.
180. Connor JR, Benkovic SA. Iron regulation in the brain: Histochemical, biochemical, and molecular considerations. *Ann Neurol Off*. 1992;32(S1):S51-S61.
181. Turati L, Moscatelli M, Mastropietro A, *et al*. *In vivo* quantitative magnetization transfer imaging correlates with histology during de- and remyelination in cuprizone-treated mice. *NMR Biomed*. 2015;28:327-337.
182. Underhill HR, Rostomily RC, Mikheev AM, Yuan C, Yarnykh VL. Fast bound pool fraction imaging of the *in vivo* rat brain: Association with myelin content and validation in the C6 glioma model. *Neuroimage*. 2011;54:2052-2065.
183. Soustelle L, Antal MC, Lamy J, Rousseau F, Armspach J, Loureiro de Sousa P. Correlations of quantitative MRI metrics with myelin basic protein (MBP) staining in a murine model of demyelination. *NMR Biomed*. 2019;32:e4116.
184. Bagnato F, Franco G, Ye F, *et al*. Selective inversion recovery quantitative magnetization transfer imaging: Toward a 3 T clinical application in multiple sclerosis. *Mult Scler J*. 2020;26:457-467.
185. Bagnato F, Hametner S, Franco G, *et al*. Selective inversion recovery quantitative magnetization transfer brain MRI at 7T: Clinical and postmortem validation in multiple sclerosis. *J Neuroimaging*. 2018;28:380-388.
186. Portnoy S, Stanisz GJ. Modeling pulsed magnetization transfer. *Magn Reson Med*. 2007;58:144-155.
187. Khodanovich MY, Kisel AA, Akulov AE, *et al*. Quantitative assessment of demyelination in ischemic stroke *in vivo* using macromolecular proton fraction mapping. *J Cereb Blood Flow Metab*. 2018;38:919-931.
188. Ramani A, Dalton C, Miller DH, Tofts PS, Barker GJ. Precise estimate of fundamental *in-vivo* MT parameters in human brain in clinically feasible times. *Magn Reson Imaging*. 2002;20:721-731.
189. Cercignani M, Barker GJ. A comparison between equations describing *in vivo* MT: The effects of noise and sequence parameters. *J Magn Reson*. 2008;191:171-183.
190. Munsch F, Varma G, Taso M, *et al*. Characterization of the cortical myeloarchitecture with inhomogeneous magnetization transfer imaging (ihMT). *Neuroimage*. 2021;225:117442.
191. Helms G, Dathe H, Kallenberg K, Dechent P. High-resolution maps of magnetization transfer with inherent correction for RF inhomogeneity and T_1 relaxation obtained from 3D FLASH MRI. *Magn Reson Med*. 2008;60:1396-1407.
192. Morris SR, Frederick R, MacKay AL, Laule C, Michal CA. Orientation dependence of inhomogeneous magnetization transfer and dipolar order relaxation rate in phospholipid bilayers. *J Magn Reson*. 2022;338:107205.
193. Van Obberghen E, Mchinda S, Le Troter A, *et al*. Evaluation of the sensitivity of inhomogeneous magnetization transfer (ihMT) MRI for multiple sclerosis. *Am J Neuroradiol*. 2018;39:634-641.
194. Harkins KD, Valentine WM, Gochberg DF, Does MD. *In-vivo* multi-exponential T_2, magnetization transfer and quantitative histology in a rat model of intramyelinic edema. *NeuroImage Clin*. 2013;2:810-817.
195. Laule C, Leung E, Li DKB, *et al*. Myelin water imaging in multiple sclerosis: Quantitative correlations with histopathology. *Mult Scler*. 2006;12:747-753.
196. Laule C, Kozlowski P, Leung E, Li DKB, MacKay AL, Moore GRW. Myelin water imaging of multiple sclerosis at 7 T: Correlations with histopathology. *Neuroimage*. 2008;40:1575-1580.
197. Chen HS-M, Holmes N, Liu J, Tetzlaff W, Kozlowski P. Validating myelin water imaging with transmission electron microscopy in a rat spinal cord injury model. *Neuroimage*. 2017;153:122-130.
198. Jelescu IO, Zurek M, Winters KV, *et al*. *In vivo* quantification of demyelination and recovery using compartment-specific diffusion MRI metrics validated by electron microscopy. *Neuroimage*. 2016;132:104-114.
199. Aboitiz F, Scheibel AB, Fisher RS, Zaidel E. Fiber composition of the human corpus callosum. *Brain Res*. 1992;598(1-2):143-153.
200. Aboitiz F, Rodriguez E, Olivares R, Zaidel E. Age-related changes in fibre composition of the human corpus callosum: Sex differences. *Neuroreport*. 1996;7:1761-1764.
201. Miller DJ, Duka T, Stimpson CD, *et al*. Prolonged myelination in human neocortical evolution. *Proc Natl Acad Sci USA*. 2012;109:16480-16485.
202. Wright AD, Jarrett M, Vavasour I, *et al*. Myelin water fraction is transiently reduced after a single mild traumatic brain injury–

A prospective cohort study in collegiate hockey players. *PLoS ONE*. 2016;11:e0150215.
203. Donovan V, Kim C, Anugerah AK, *et al*. Repeated mild traumatic brain injury results in long-term white-matter disruption. *J Cereb Blood Flow Metab Off J Int Soc Cereb Blood Flow Metab*. 2014;34:715-723.
204. Kolind S, Abel S, Taylor C, *et al*. Myelin water imaging in relapsing multiple sclerosis treated with ocrelizumab and interferon beta-1a. *NeuroImage Clin*. 2022;35:103109.
205. Lin M, Zhang J, Zhang Y, Luo J, Shi S. Ocrelizumab for multiple sclerosis. *Cochrane Database Syst Rev*. 2022;5:1–56.
206. Montalban X, Hauser SL, Kappos L, *et al*. Ocrelizumab versus placebo in primary progressive multiple sclerosis. *N Engl J Med*. 2017;376:209-220.
207. Dvorak AV, Swift-LaPointe T, Vavasour IM, *et al*. An atlas for human brain myelin content throughout the adult life span. *Sci Rep*. 2021;11:1-13.
208. Baumeister TR, Lin S-J, Vavasour I, *et al*. Data fusion detects consistent relations between non-lesional white matter myelin, executive function, and clinical characteristics in multiple sclerosis. *NeuroImage Clin*. 2019;24:101926.
209. Vavasour IM, Tam R, Li DKB, *et al*. A 24-month advanced magnetic resonance imaging study of multiple sclerosis patients treated with alemtuzumab. *Mult Scler J*. 2019;25:811-818.
210. Abel S, Vavasour I, Lee LE, *et al*. Associations between findings from myelin water imaging and cognitive performance among individuals with multiple sclerosis. *JAMA Netw open*. 2020;3:e2014220.
211. Dula AN, Gochberg DF, Valentine HL, Valentine WM, Does MD. Multiexponential T_2, magnetization transfer, and quantitative histology in white matter tracts of rat spinal cord. *Magn Reson Med*. 2010;63:902-909.
212. Dortch RD, Harkins KD, Juttukonda MR, Gore JC, Does MD. Characterizing inter-compartmental water exchange in myelinated tissue using relaxation exchange spectroscopy. *Magn Reson Med*. 2013;70:1450-1459.
213. Lodygensky GA, Marques JP, Maddage R, *et al*. *In vivo* assessment of myelination by phase imaging at high magnetic field. *Neuroimage*. 2012;59:1979-1987.
214. Argyridis I, Li W, Johnson GA, Liu C. Quantitative magnetic susceptibility of the developing mouse brain reveals microstructural changes in the white matter. *Neuroimage*. 2014;88:134-142.
215. Wiggermann V, Hametner S, Hernández-Torres E, *et al*. Susceptibility-sensitive MRI of multiple sclerosis lesions and the impact of normal-appearing white matter changes. *NMR Biomed*. 2017;30:e3727.
216. Fukunaga M, Li T-Q, van Gelderen P, *et al*. Layer-specific variation of iron content in cerebral cortex as a source of MRI contrast. *Proc Natl Acad Sci USA*. 2010;107:3834-3839.
217. Duyn JH, Schenck J. Contributions to magnetic susceptibility of brain tissue. *NMR Biomed*. 2017;30:e3546.
218. Duyn JH, van Gelderen P, Li T-Q, de Zwart JA, Koretsky AP, Fukunaga M. High-field MRI of brain cortical substructure based on signal phase. *Proc Natl Acad Sci USA*. 2007;104:11796-11801.
219. Gudbjartsson H, Patz S. The Rician distribution of noisy MRI data. *Magn Reson Med*. 1995;34:910-914.
220. Liu C. Susceptibility tensor imaging. *Magn Reson Med*. 2010;63:1471-1477.
221. Li W, Wu B, Avram AV, Liu C. Magnetic susceptibility anisotropy of human brain in vivo and its molecular underpinnings. *Neuroimage*. 2012;59:2088-2097.
222. Reichenbach JR, Venkatesan R, Schillinger DJ, Kido DK, Haacke EM. Small vessels in the human brain: MR venography with deoxyhemoglobin as an intrinsic contrast agent. *Radiology*. 1997;204:272-277.
223. Kor D, Birkl C, Ropele S, *et al*. The role of iron and myelin in orientation dependent R_2^* of white matter. *NMR Biomed*. 2019;32:e4092.
224. Hernández-Torres E, Wiggermann V, Hametner S, *et al*. Orientation dependent MR signal decay differentiates between people with MS, their asymptomatic siblings and unrelated healthy controls. *PLoS ONE*. 2015;10:e0140956.
225. Khalil M, Langkammer C, Pichler A, *et al*. Dynamics of brain iron levels in multiple sclerosis: A longitudinal 3T MRI study. *Neurology*. 2015;84:2396-2402.
226. Sati P, Oh J, Constable RT, *et al*. The central vein sign and its clinical evaluation for the diagnosis of multiple sclerosis: A consensus statement from the north American imaging in multiple sclerosis cooperative. *Nat Rev Neurol*. 2016;12:714-722.
227. Absinta M, Sati P, Schindler M, *et al*. Persistent 7-tesla phase rim predicts poor outcome in new multiple sclerosis patient lesions. *J Clin Invest*. 2016;126:2597-2609.
228. Dal-Bianco A, Grabner G, Kronnerwetter C, *et al*. Slow expansion of multiple sclerosis iron rim lesions: Pathology and 7 T magnetic resonance imaging. *Acta Neuropathol*. 2017;133:25-42.
229. Wang C, Martins-Bach AB, Alfaro-Almagro F, *et al*. Phenotypic and genetic associations of quantitative magnetic susceptibility in UK biobank brain imaging. *Nat Neurosci*. 2022;25:818–831.
230. Weber AM, Zhang Y, Kames C, Rauscher A. Myelin water imaging and R_2^* mapping in neonates: Investigating R_2^* dependence on myelin and fibre orientation in whole brain white matter. *NMR Biomed*. 2020;33:e4222.
231. Brody BA, Kinney HC, Kloman AS, Gilles FH. Sequence of central nervous system myelination in human infancy. I. An autopsy study of myelination. *J Neuropathol Exp Neurol*. 1987;46:283-301.
232. Zhang Y, Shi J, Wei H, Han V, Zhu W-Z, Liu C. Neonate and infant brain development from birth to 2 years assessed using MRI-based quantitative susceptibility mapping. *Neuroimage*. 2019;185:349-360.
233. Guglielmetti C, Boucneau T, Cao P, Van der Linden A, Larson PEZ, Chaumeil MM. Longitudinal evaluation of demyelinated lesions in a multiple sclerosis model using ultrashort echo time magnetization transfer (UTE-MT) imaging. *Neuroimage*. 2020;208:116415.
234. Guglielmetti C, Le Blon D, Santermans E, *et al*. Interleukin-13 immune gene therapy prevents CNS inflammation and demyelination via alternative activation of microglia and macrophages. *Glia*. 2016;64:2181-2200.
235. Ouellette R, Mangeat G, Polyak I, *et al*. Validation of rapid magnetic resonance myelin imaging in multiple sclerosis. *Ann Neurol*. 2020;87:710-724.
236. Saccenti L, Andica C, Hagiwara A, *et al*. Brain tissue and myelin volumetric analysis in multiple sclerosis at 3T MRI with various in-plane resolutions using synthetic MRI. *Neuroradiology*. 2019;61:1219-1227.
237. Schmidbauer V, Geisl G, Diogo M, *et al*. SyMRI detects delayed myelination in preterm neonates. *Eur Radiol*. 2019;29:7063-7072.
238. Kim HG, Moon W-J, Han J, Choi JW. Quantification of myelin in children using multiparametric quantitative MRI: A pilot study. *Neuroradiology*. 2017;59:1043-1051.
239. de Paula Faria D, de Vries EF, Sijbesma JW, Buchpiguel CA, Dierckx RA, Copray SC. PET imaging of glucose metabolism, neuroinflammation and demyelination in the lysolecithin rat model for multiple sclerosis. *Mult Scler J*. 2014;20:1443-1452.

240. Bodini B, Tonietto M, Airas L, *et al*. Positron emission tomography in multiple sclerosis — straight to the target. *Nat Rev Neurol*. 2022;17:663-675.
241. Pietroboni AM, Carandini T, Colombi A, *et al*. Amyloid PET as a marker of normal-appearing white matter early damage in multiple sclerosis: Correlation with CSF β-amyloid levels and brain volumes. *Eur J Nucl Med Mol Imaging*. 2019;46:280-287.
242. Grecchi E, Veronese M, Bodini B, *et al*. Multimodal partial volume correction: Application to [^{11}C] PIB PET/MRI myelin imaging in multiple sclerosis. *J Cereb Blood Flow Metab*. 2017;37:3803-3817.
243. Matías-Guiu JA, Cabrera-Martín MN, Cortés-Martínez A, *et al*. Amyloid PET in pseudotumoral multiple sclerosis. *Mult Scler Relat Disord*. 2017;15:15-17.
244. Jung W, Lee J, Shin H-G, *et al*. Whole brain *g*-ratio mapping using myelin water imaging (MWI) and neurite orientation dispersion and density imaging (NODDI). *Neuroimage*. 2018;182:379-388.
245. Janve VA, Zu Z, Yao SY, *et al*. The radial diffusivity and magnetization transfer pool size ratio are sensitive markers for demyelination in a rat model of type III multiple sclerosis (MS) lesions. *Neuroimage*. 2013;74:298-305.
246. Thiessen JD, Zhang Y, Zhang H, *et al*. Quantitative MRI and ultrastructural examination of the cuprizone mouse model of demyelination. *NMR Biomed*. 2013;26:1562-1581.
247. Khodanovich MY, Sorokina IV, Glazacheva VY, *et al*. Histological validation of fast macromolecular proton fraction mapping as a quantitative myelin imaging method in the cuprizone demyelination model. *Sci Rep*. 2017;7:46686.
248. Khodanovich M, Pishchelko A, Glazacheva V, *et al*. Quantitative imaging of white and gray matter remyelination in the cuprizone demyelination model using the macromolecular proton fraction. *Cells*. 2019;8:1204.
249. Deloire-Grassin MSA, Brochet B, Quesson B, *et al*. *In vivo* evaluation of remyelination in rat brain by magnetization transfer imaging. *J Neurol Sci*. 2000;178:10-16.
250. Merkler D, Boretius S, Stadelmann C, *et al*. Multicontrast MRI of remyelination in the central nervous system. *NMR Biomed*. 2005;18:395-403.
251. Zaaraoui W, Deloire M, Merle M, *et al*. Monitoring demyelination and remyelination by magnetization transfer imaging in the mouse brain at 9.4 T. *Magn Reson Mater Physics, Biol Med*. 2008;21:357-362.
252. Fjær S, Bø L, Myhr KM, Torkildsen O, Wergeland S. Magnetization transfer ratio does not correlate to myelin content in the brain in the MOG-EAE mouse model. *Neurochem Int*. 2015;83-84:28-40.
253. Lehto LJ, Albors AA, Sierra A, *et al*. Lysophosphatidyl choline induced demyelination in rat probed by relaxation along a fictitious field in high rank rotating frame. *Front Neurosci*. 2017;11:433.
254. Lehto LJ, Sierra A, Gröhn O. Magnetization transfer SWIFT MRI consistently detects histologically verified myelin loss in the thalamocortical pathway after a traumatic brain injury in rat. *NMR Biomed*. 2017;30:1–13.
255. Tardif CL, Bedell BJ, Eskildsen SF, Collins DL, Pike GB. Quantitative magnetic resonance imaging of cortical multiple sclerosis pathology. *Mult Scler Int*. 2012;2012:1-13.
256. Reeves C, Tachrount M, Thomas D, *et al*. Combined *ex vivo* 9.4T MRI and quantitative histopathological study in normal and pathological neocortical resections in focal epilepsy. *Brain Pathol*. 2016;26:319-333.
257. Bagnato F, Hametner S, Boyd E, *et al*. Untangling the R2* contrast in multiple sclerosis: A combined MRI-histology study at 7.0 tesla. *PLoS ONE*. 2018;13:e0193839.
258. Duval T, Smith V, Stikov N, Klawiter EC, Cohen-Adad J. Scan–rescan of axcaliber, macromolecular tissue volume, and *g*-ratio in the spinal cord. *Magn Reson Med*. 2018;79:2759-2765.
259. Feng X, Deistung A, Reichenbach JR. Quantitative susceptibility mapping (QSM) and R2* in the human brain at 3 T: Evaluation of intra-scanner repeatability. *Z Med Phys*. 2018;28:36-48.
260. Drenthen GS, Backes WH, Aldenkamp AP, Jansen JFA. Applicability and reproducibility of 2D multi-slice GRASE myelin water fraction with varying acquisition acceleration. *Neuroimage*. 2019;195:333-339.
261. Zhang L, Chen T, Tian H, *et al*. Reproducibility of inhomogeneous magnetization transfer (ihMT): A test-retest, multi-site study. *Magn Reson Imaging*. 2019;57:243-249.
262. Wu Y, Alexander AL, Fleming JO, Duncan ID, Field AS. Myelin water fraction in human cervical spinal cord *in vivo*. *J Comput Assist Tomogr*. 2006;30:304-306.
263. Meyers SM, Laule C, Vavasour IM, *et al*. Reproducibility of myelin water fraction analysis: A comparison of region of interest and voxel-based analysis methods. *Magn Reson Imaging*. 2009;27:1096-1103.
264. Levesque IR, Chia CLL, Pike GB. Reproducibility of *in vivo* magnetic resonance imaging-based measurement of myelin water. *J Magn Reson Imaging*. 2010;32:60-68.
265. Nguyen TD, Deh K, Monohan E, *et al*. Feasibility and reproducibility of whole brain myelin water mapping in 4 minutes using fast acquisition with spiral trajectory and adiabatic T_2prep (FAST-T_2) at 3T. *Magn Reson Med*. 2016;76:456-465.
266. Ellerbrock I, Mohammadi S. Four *in vivo g*-ratio-weighted imaging methods: Comparability and repeatability at the group level. *Hum Brain Mapp*. 2018;39:24-41.
267. Ljungberg E, Vavasour I, Tam R, *et al*. Rapid myelin water imaging in human cervical spinal cord. *Magn Reson Med*. 2017;78:1482-1487.
268. Lévy S, Guertin M-C, Khatibi A, *et al*. Test-retest reliability of myelin imaging in the human spinal cord: Measurement errors versus region-and aging-induced variations. *PLoS ONE*. 2018;13:e0189944.
269. Lancione M, Tosetti M, Donatelli G, Cosottini M, Costagli M. The impact of white matter fiber orientation in single-acquisition quantitative susceptibility mapping. *NMR Biomed*. 2017;30:e3798.
270. Pampel A, Müller DK, Anwander A, Marschner H, Möller HE. Orientation dependence of magnetization transfer parameters in human white matter. *Neuroimage*. 2015;114:136-146.
271. Denk C, Hernandez Torres E, MacKay A, Rauscher A. The influence of white matter fibre orientation on MR signal phase and decay. *NMR Biomed*. 2011;24:246-252.
272. Hagiwara A, Hori M, Yokoyama K, *et al*. Analysis of white matter damage in patients with multiple sclerosis via a novel *in vivo* MR method for measuring myelin, axons, and G-ratio. *AJNR Am J Neuroradiol*. 2017;38:1934-1940.
273. Yu F, Fan Q, Tian Q, *et al*. Imaging G-ratio in multiple sclerosis using high-gradient diffusion MRI and macromolecular tissue volume. *Am J Neuroradiol*. 2019;40:1871-1877.
274. Chen W, Gauthier SA, Gupta A, *et al*. Quantitative susceptibility mapping of multiple sclerosis lesions at various ages. *Radiology*. 2014;271:183-192.
275. Wiggermann V, Hernández Torres E, Vavasour IM, *et al*. Magnetic resonance frequency shifts during acute MS lesion formation. *Neurology*. 2013;81:211-218.
276. Filippi M, Rocca MA, Martino G, Horsfield MA, Comi G. Magnetization transfer changes in the normal appearing white matter precede the appearance of enhancing lesions in patients with multiple sclerosis. *Ann Neurol*. 1998;43:809-814.

277. Yablonskiy DA, Luo J, Sukstanskii AL, Iyer A, Cross AH. Biophysical mechanisms of MRI signal frequency contrast in multiple sclerosis. *Proc Natl Acad Sci USA*. 2012;109:14212-14217.
278. Shmueli K, Dodd SJ, Li T, Duyn JH. The contribution of chemical exchange to MRI frequency shifts in brain tissue. *Magn Reson Med*. 2011;65:35-43.
279. Kaunzner UW, Kang Y, Zhang S, *et al*. Quantitative susceptibility mapping identifies inflammation in a subset of chronic multiple sclerosis lesions. *Brain*. 2019;142:133-145.
280. Deh K, Ponath GD, Molvi Z, *et al*. Magnetic susceptibility increases as diamagnetic molecules breakdown: Myelin digestion during multiple sclerosis lesion formation contributes to increase on QSM. *J Magn Reson Imaging*. 2018;48:1281-1287.
281. Maggi P, Sati P, Nair G, *et al*. Paramagnetic rim lesions are specific to multiple sclerosis: An international multicenter 3T MRI study. *Ann Neurol*. 2020;88:1034-1042.
282. Rudko DA, Solovey I, Gati JS, Kremenchutzky M, Menon RS. Multiple sclerosis: Improved identification of disease-relevant changes in gray and white matter by using susceptibility-based MR imaging. *Radiology*. 2014;272:851-864.
283. Cronin MJ, Wharton S, Al-Radaideh A, *et al*. A comparison of phase imaging and quantitative susceptibility mapping in the imaging of multiple sclerosis lesions at ultrahigh field. *MAGMA*. 2016;29:543-557.
284. Chen W, Zhang Y, Mu K, *et al*. Quantifying the susceptibility variation of normal-appearing white matter in multiple sclerosis by quantitative susceptibility mapping. *AJR Am J Roentgenol*. 2017;209:889-894.
285. Rasoanandrianina H, Demortière S, Trabelsi A, *et al*. Sensitivity of the inhomogeneous magnetization transfer imaging technique to spinal cord damage in multiple sclerosis. *AJNR Am J Neuroradiol*. 2020;41:929-937.
286. Weber AM, Pukropski A, Kames C, *et al*. Pathological insights from quantitative susceptibility mapping and diffusion tensor imaging in ice hockey players pre and post-concussion. *Front Neurol*. 2018;9:575.
287. Flechsig PE. *Anatomie des menschlichen gehirns und rückenmarks auf myelogenetischer grundlage*. *Vol*. 1. Leipzig: G. Thieme; 1920.
288. Van Essen DC. Corticocortical and thalamocortical information flow in the primate visual system. *Prog Brain Res*. 2005; 149:173-185.
289. Kaas JH, Collins CE. The organization of sensory cortex. *Curr Opin Neurobiol*. 2001;11:498-504.
290. Meier-Ruge W, Ulrich J, Brühlmann M, Meier E. Age-related white matter atrophy in the human brain. *Ann N Y Acad Sci*. 1992;673:260-269.
291. Marner L, Pakkenberg B. Total length of nerve fibers in prefrontal and global white matter of chronic schizophrenics. *J Psychiatr Res*. 2003;37:539-547.
292. Whitaker KJ, Kolind SH, MacKay AL, Clark CM. Quantifying development: Investigating highly myelinated voxels in preadolescent corpus callosum. *Neuroimage*. 2008;43:731-735.
293. Tang X, Zhang H, Zhou J, *et al*. Brain development in children with developmental delay using amide proton transfer-weighted imaging and magnetization transfer imaging. *Pediatr Investig*. 2020;4:250-256.
294. Taso M, Girard OM, Duhamel G, *et al*. Tract-specific and age-related variations of the spinal cord microstructure: A multi-parametric MRI study using diffusion tensor imaging (DTI) and inhomogeneous magnetization transfer (ihMT). *NMR Biomed*. 2016;29:817-832.
295. Bilgic B, Pfefferbaum A, Rohlfing T, Sullivan EV, Adalsteinsson E. MRI estimates of brain iron concentration in normal aging using quantitative susceptibility mapping. *Neuroimage*. 2012; 59:2625-2635.
296. Dean DC III, O'Muircheartaigh J, Dirks H, *et al*. Mapping an index of the myelin g-ratio in infants using magnetic resonance imaging. *Neuroimage*. 2016;132:225-237.
297. Cercignani M, Giulietti G, Dowell NG, *et al*. Characterizing axonal myelination within the healthy population: A tract-by-tract mapping of effects of age and gender on the fiber g-ratio. *Neurobiol Aging*. 2017;49:109-118.
298. Berman S, West KL, Does MD, Yeatman JD, Mezer AA. Evaluating *g*-ratio weighted changes in the corpus callosum as a function of age and sex. *Neuroimage*. 2018;182:304-313.
299. Dubois J, Dehaene-Lambertz G, Kulikova S, Poupon C, Hüppi PS, Hertz-Pannier L. The early development of brain white matter: A review of imaging studies in fetuses, newborns and infants. *Neuroscience*. 2014;276:48-71.
300. Flynn SW, Lang DJ, Mackay AL, *et al*. Abnormalities of myelination in schizophrenia detected *in vivo* with MRI, and post-mortem with analysis of oligodendrocyte proteins. *Mol Psychiatry*. 2003;8:811-820.
301. Borich MR, Mackay AL, Vavasour IM, Rauscher A, Boyd LA. Evaluation of white matter myelin water fraction in chronic stroke. *NeuroImage Clin*. 2013;2:569-580.
302. Chen G, Fu S, Chen P, *et al*. Reduced myelin density in unmedicated major depressive disorder: An inhomogeneous MT MRI study. *J Affect Disord*. 2022;300:114-120.
303. Parlak S, Coban G, Gumeler E, *et al*. Reduced myelin in patients with isolated hippocampal sclerosis as assessed by SyMRI. *Neuroradiology*. 2022;64:99-107.
304. Park M, Moon Y, Han S-H, Kim HK, Moon W-J. Myelin loss in white matter hyperintensities and normal-appearing white matter of cognitively impaired patients: A quantitative synthetic magnetic resonance imaging study. *Eur Radiol*. 2019;29: 4914-4921.
305. Bourbon-Teles J, Bells S, Jones DK, Coulthard E, Rosser A, Metzler-Baddeley C. Myelin breakdown in human Huntington's disease: Multi-modal evidence from diffusion MRI and quantitative MT. *Neuroscience*. 2019;403:79-92.
306. Zikou A, Ioannidou M-C, Tzoufi M, Astrakas L, Argyropoulou MI. Magnetization transfer ratio measurements of the brain in children with tuberous sclerosis complex. *Pediatr Radiol*. 2005;35:1071-1074.
307. Maleki S, Chye Y, Zhang X, *et al*. Neural correlates of symptom severity in obsessive-compulsive disorder using magnetization transfer and diffusion tensor imaging. *Psychiatry Res Neuroimaging*. 2020;298:111046.
308. Hou G, Lai W, Jiang W, *et al*. Myelin deficits in patients with recurrent major depressive disorder: An inhomogeneous magnetization transfer study. *Neurosci Lett*. 2021;750:135768.
309. Billiet T, Mädler B, D'Arco F, *et al*. Characterizing the microstructural basis of "unidentified bright objects" in neurofibromatosis type 1: A combined *in vivo* multicomponent T_2 relaxation and multi-shell diffusion MRI analysis. *NeuroImage Clin*. 2014;4:649-658.
310. Coban G, Parlak S, Gumeler E, *et al*. Synthetic MRI in neurofibromatosis type 1. *AJNR Am J Neuroradiol*. 2021;42:1709-1715.
311. de Paula Faria D, Vlaming MLH, Copray SCVM, *et al*. PET Imaging of disease progression and treatment effects in the experimental autoimmune encephalomyelitis rat model. *J Nucl Med*. 2014;55:1330-1336.
312. Boellaard R, Delgado-Bolton R, Oyen WJG, *et al*. FDG PET/CT: EANM procedure guidelines for tumour imaging: Version 2.0. *Eur J Nucl Med Mol Imaging*. 2015;42:328-354.
313. Takikawa S, Dhawan V, Spetsieris P, *et al*. Noninvasive quantitative fluorodeoxyglucose PET studies with an estimated input function derived from a population-based arterial blood curve. *Radiology*. 1993;188:131-136.

314. Chen K, Bandy D, Reiman E, *et al*. Noninvasive quantification of the cerebral metabolic rate for glucose using positron emission tomography, ^{18}F-fluoro-2-deoxyglucose, the Patlak method, and an image-derived input function. *J Cereb Blood Flow Metab*. 1998;18:716-723.
315. Feng D, Huang SC, Wang X. Models for computer simulation studies of input functions for tracer kinetic modeling with positron emission tomography. *Int J Biomed Comput*. 1993;32: 95-110.
316. Jang H, Ma Y, Searleman AC, *et al*. Inversion recovery UTE based volumetric myelin imaging in human brain using interleaved hybrid encoding. *Magn Reson Med*. 2020;83:950-961.
317. Labadie C, Lee J-H, Rooney WD, *et al*. Myelin water mapping by spatially regularized longitudinal relaxographic imaging at high magnetic fields. *Magn Reson Med*. 2014;71:375-387.
318. Liu H, Rubino C, Dvorak AV, *et al*. Myelin water atlas: A template for myelin distribution in the brain. *J Neuroimaging*. 2019;29:699-706.
319. Morris SR, Holmes RD, Dvorak AV, *et al*. Brain myelin water fraction and diffusion tensor imaging atlases for 9-10 year-old children. *J Neuroimaging*. 2020;30:150-160.
320. Liu Y, Leong ATL, Zhao Y, *et al*. A low-cost and shielding-free ultra-low-field brain MRI scanner. *Nat Commun*. 2021;12: 7238.
321. Mickevicius NJ, Kim JP, Zhao J, Morris ZS, Hurst NJJ, Glide-Hurst CK. Toward magnetic resonance fingerprinting for low-field MR-guided radiation therapy. *Med Phys*. 2021;48:6930-6940.
322. Ma D, Gulani V, Seiberlich N, *et al*. Magnetic resonance fingerprinting. *Nature*. 2013;495:187-192.
323. Bipin Mehta B, Coppo S, Frances McGivney D, *et al*. Magnetic resonance fingerprinting: A technical review. *Magn Reson Med*. 2019;81:25-46.
324. Panda A, Mehta BB, Coppo S, *et al*. Magnetic resonance fingerprinting-an overview. *Curr Opin Biomed Eng*. 2017;3:56-66.
325. Kiselev VG, Körzdörfer G, Gall P. Toward quantification: Microstructure and magnetic resonance fingerprinting. *Invest Radiol*. 2021;56:1-9.
326. Chen Y, Chen M-H, Baluyot KR, Potts TM, Jimenez J, Lin W. MR Fingerprinting enables quantitative measures of brain tissue relaxation times and myelin water fraction in the first five years of life. *Neuroimage*. 2019;186:782-793.
327. Cui D, Hui ES, Cao P. A multi-inversion-recovery magnetic resonance fingerprinting for multi-compartment water mapping. *Magn Reson Imaging*. 2021;81:82-87.
328. Li Q, Cao X, Ye H, Liao C, He H, Zhong J. Ultrashort echo-time magnetic resonance fingerprinting (UTE-MRF) for simultaneous quantification of long and ultrashort T_2 tissues. *Magn Reson Med*. 2019;82:1359-1372.
329. Tobisch A, Stirnberg R, Harms RL, *et al*. Compressed sensing diffusion spectrum imaging for accelerated diffusion microstructure MRI in long-term population imaging. *Front Neurosci*. 2018;12:650.
330. West DJ, Cruz G, Teixeira RPAG, *et al*. An MR fingerprinting approach for quantitative inhomogeneous magnetization transfer imaging. *Magn Reson Med*. 2022;87:220-235.
331. Muthupillai R, Lomas DJ, Rossman PJ, Greenleaf JF, Manduca A, Ehman RL. Magnetic resonance elastography by direct visualization of propagating acoustic strain waves. *Science*. 1995;269: 1854-1857.
332. Murphy MC, Huston J III, Ehman RL. MR elastography of the brain and its application in neurological diseases. *Neuroimage*. 2019;187:176-183.
333. Murphy MC, Huston J III, Jack CRJ, *et al*. Decreased brain stiffness in Alzheimer's disease determined by magnetic resonance elastography. *J Magn Reson Imaging*. 2011;34:494-498.
334. McGarry MDJ, Van Houten EEW, Johnson CL, *et al*. Multiresolution MR elastography using nonlinear inversion. *Med Phys*. 2012;39:6388-6396.
335. Freimann FB, Müller S, Streitberger K-J, *et al*. MR Elastography in a murine stroke model reveals correlation of macroscopic viscoelastic properties of the brain with neuronal density. *NMR Biomed*. 2013;26:1534-1539.
336. Klein C, Hain EG, Braun J, *et al*. Enhanced adult neurogenesis increases brain stiffness: *In vivo* magnetic resonance elastography in a mouse model of dopamine depletion. *PLoS ONE*. 2014;9:e92582.
337. Hain EG, Klein C, Munder T, *et al*. Dopaminergic neurodegeneration in the mouse is associated with decrease of viscoelasticity of substantia nigra tissue. *PLoS ONE*. 2016;11:e0161179.
338. Schregel K, Wuerfel E, Garteiser P, *et al*. Demyelination reduces brain parenchymal stiffness quantified *in vivo* by magnetic resonance elastography. *Proc Natl Acad Sci U S A*. 2012;109: 6650-6655.
339. Millward JM, Guo J, Berndt D, Braun J, Sack I, Infante-Duarte C. Tissue structure and inflammatory processes shape viscoelastic properties of the mouse brain. *NMR Biomed*. 2015; 28:831-839.
340. Wuerfel J, Paul F, Beierbach B, *et al*. MR-elastography reveals degradation of tissue integrity in multiple sclerosis. *Neuroimage*. 2010;49:2520-2525.
341. Streitberger K-J, Sack I, Krefting D, *et al*. Brain viscoelasticity alteration in chronic-progressive multiple sclerosis. *PLoS ONE*. 2012;7:e29888.
342. Herthum H, Hetzer S, Scheel M, *et al*. *In vivo* stiffness of multiple sclerosis lesions is similar to that of normal-appearing white matter. *Acta Biomater*. 2022;138:410-421.
343. Cherry SR, Sorenson JA, Phelps ME. *Physics in nuclear medicine E-book*. Amsterdam: Elsevier Health Sciences; 2012.
344. Badawi RD, Shi H, Hu P, *et al*. First human imaging studies with the EXPLORER total-body PET scanner. *J Nucl Med*. 2019;60: 299-303.
345. Tsoumpas C, Turkheimer FE, Thielemans K. Study of direct and indirect parametric estimation methods of linear models in dynamic positron emission tomography. *Med Phys*. 2008; 35:1299-1309.
346. Tsoumpas C, Turkheimer FE, Thielemans K. A survey of approaches for direct parametric image reconstruction in emission tomography. *Med Phys*. 2008;35:3963-3971.
347. Cohen-Adad J, Alonso-Ortiz E, Abramovic M, *et al*. Generic acquisition protocol for quantitative MRI of the spinal cord. *Nat Protoc*. 2021;16:4611-4632.
348. Bouman PM, Steenwijk MD, Pouwels PJW, *et al*. Histopathology-validated recommendations for cortical lesion imaging in multiple sclerosis. *Brain*. 2020;143:2988-2997.
349. Heckova E, Dal-Bianco A, Strasser B, *et al*. Extensive brain pathologic alterations detected with 7.0-T MR spectroscopic imaging associated with disability in multiple sclerosis. *Radiology*. 2022;303:141-150.
350. Faizy TD, Kumar D, Broocks G, *et al*. Age-related measurements of the myelin water fraction derived from 3D multi-echo GRASE reflect myelin content of the cerebral white matter. *Sci Rep*. 2018;8:1-8.
351. Nossin-Manor R, Card D, Raybaud C, Taylor MJ, Sled JG. Cerebral maturation in the early preterm period—A magnetization transfer and diffusion tensor imaging study using voxel-based analysis. *Neuroimage*. 2015;112:30-42.
352. Engelbrecht V, Rassek M, Preiss S, Wald C, Mödder U. Age-dependent changes in magnetization transfer contrast of white matter in the pediatric brain. *Am J Neuroradiol*. 1998; 19:1923-1929.

353. Chen J, Gong NJ, Chaim KT, Otaduy MCG, Liu C. Decompose quantitative susceptibility mapping (QSM) to sub-voxel diamagnetic and paramagnetic components based on gradient-echo MRI data. *Neuroimage* 2021;242: 118477.
354. Shin HG, Lee J, Yun YH, *et al*. χ-separation: Magnetic susceptibility source separation toward iron and myelin mapping in the brain. *Neuroimage* 2021;240:118371.
355. Kim W, Shin HG, Lee H, *et al*. χ-Separation imaging for diagnosis of multiple sclerosis versus neuromyelitis optica spectrum disorder. *Radiology*. 2023;307:e220941.
356. Emmerich J, Bachert P, Ladd ME, Straub S. On the separation of susceptibility sources in quantitative susceptibility mapping: Theory and phantom validation with an in vivo application to multiple sclerosis lesions of different age. *J Magn Reson*. 2021;330:107033.